

JWST’s PEARLS: A $z \simeq 6$ Quasar in a Train-Wreck Galaxy Merger System

Madeline A. Marshall^{*1}, Rogier A. Windhorst², Giovanni Ferrami^{3,4}, S. P. Willner⁵, Maria Polletta⁶, William C. Keel⁷, Giovanni G. Fazio⁸, Seth H. Cohen², Timothy Carleton², Rolf A. Jansen², Rachel Honor², Rafael Ortiz III², Jake Summers², Jordan C. J. D’Silva^{9,4}, Anton M. Koekemoer¹⁰, Dan Coe^{10,11,12}, Christopher J. Conselice¹³, Jose M. Diego¹⁴, Simon P. Driver⁹, Brenda Frye¹⁵, Norman A. Grogin¹⁰, Nor Pirzkal¹⁰, Aaron Robotham⁹, Russell E. Ryan, Jr.¹⁰, Christopher N. A. Willmer¹⁶, Haojing Yan¹⁷, Massimo Ricotti¹⁸, Adi Zitrin¹⁹, Nathan J. Adams²⁰, Cheng Cheng²¹, J. Stuart B. Wyithe^{22,4}, Jeremy Lim²³, Michele Perna²⁴, Hannah Übler²⁵, Chris J. Willott²⁶, Gareth Jones^{27,28}, Jan Scholtz^{27,28}, and Mira Mechtley²

(Affiliations can be found after the references)

March 3, 2025

ABSTRACT

We present JWST NIRSpec integral field spectroscopy observations of the $z = 5.89$ quasar NDWFS J1425+3254 from 0.6–5.3 μm , covering the rest-frame ultraviolet and optical at spectral resolution $R \sim 100$. The quasar has a black hole mass of $M_{\text{BH}} = (1.4^{+3.1}_{-1.0}) \times 10^9 M_{\odot}$ and an Eddington ratio $L_{\text{Bol}}/L_{\text{Edd}} = 0.3^{+0.6}_{-0.2}$, as implied from the broad Balmer $H\alpha$ and $H\beta$ lines. We find that the quasar host has significant ongoing obscured star formation, as well as a quasar-driven outflow with velocity $6050^{+460}_{-630} \text{ km s}^{-1}$, possibly one of the most extreme outflows in the early Universe. The IFU data also reveals that two companion galaxies are merging with the quasar host. The north-eastern companion galaxy is relatively old and very massive, with luminosity-weighted stellar age 65^{+9}_{-4} Myr , stellar mass $(3.6^{+0.6}_{-0.3}) \times 10^{11} M_{\odot}$, and $\text{SFR} < (16.1 \pm 1.9) M_{\odot} \text{ yr}^{-1}$. A bridge of gas connects this companion galaxy and the host, confirming their ongoing interaction. A second merger is occurring between the quasar host and a much younger companion galaxy to the south, with stellar age $6.7 \pm 1.8 \text{ Myr}$, stellar mass $(1.9 \pm 0.4) \times 10^{10} M_{\odot}$, and $\text{SFR} < (93^{+17}_{-16}) M_{\odot} \text{ yr}^{-1}$. There is also another galaxy in the field that is likely in the foreground at $z = 1.135$, that could be gravitationally lensing the quasar with magnification $1 < \mu < 2$, and so $< 0.75 \text{ mag}$. Overall, the system is a “train-wreck” merger of three galaxies, with star formation and extreme quasar activity that were likely triggered by these ongoing interactions.

Key words. quasars: supermassive black holes – quasars: emission lines – Galaxies: high-redshift – Galaxies: interactions – Galaxies: active

1. Introduction

Hundreds of quasars within the first billion years of the Universe’s history have been discovered using large sky surveys (e.g., Fan et al. 2000, 2001, 2003; Willott et al. 2009, 2010; Kashikawa et al. 2015; Bañados et al. 2016, 2018, 2022; Matsuoka et al. 2018; Wang et al. 2019; Yang et al. 2023). These $z \gtrsim 6$ quasars are powered by intense accretion at or even above the Eddington limit (Willott et al. 2010; De Rosa et al. 2011; Zappacosta et al. 2023) onto supermassive black holes with masses of up to a few times $10^9 M_{\odot}$ (Barth et al. 2003; Jiang et al. 2007; Kurk et al. 2007; De Rosa et al. 2011; Yang et al. 2020). These quasars raise the question of how these black holes first formed and grew so rapidly.

One theory is that these rare quasars live in the rarest, most massive, dark-matter haloes. These haloes formed in high-density environments where gas can be efficiently funnelled into galaxies along gas filaments, which could fuel extreme black hole growth. However, observations have yet to show whether quasars live in the most massive haloes, with some surveys searching for protocluster-scale galaxy overdensities around high- z quasars finding overdensities (e.g., Stiavelli et al. 2005; Zheng et al. 2006; Morselli et al. 2014; Mignoli et al. 2020) while others find no evidence that quasars reside in higher-density regions (e.g., Willott

et al. 2005; Bañados et al. 2013; Simpson et al. 2014; Goto et al. 2017). This picture has not yet become clearer even with the James Webb Space Telescope (JWST; Gardner et al. 2006, 2023; McElwain et al. 2023), as observations have found quasars in a wide range of environments (e.g., Kashino et al. 2023; Wang et al. 2023; Eilers et al. 2024; Champagne et al. 2024).

Some theories suggest that local—kpc-scale—interactions can be physical triggers for active galactic nuclei (AGN) and black hole growth (e.g., Sanders et al. 1988; Hopkins et al. 2006). Observations at low- z indeed find that mergers drive some AGN activity (e.g. Ellison et al. 2011; Bessiere et al. 2012; Glikman et al. 2015; Araujo et al. 2023). For example, low- z Seyfert galaxies have tidal disturbances in their H I gas at much higher rates than similar inactive galaxies (Lim & Ho 1999; Kuo et al. 2008; Tang et al. 2008). However, interactions are not ubiquitously observed to be fuelling low- z quasar hosts (Cisternas et al. 2011; Kocevski et al. 2012; Mechtley et al. 2016; Marian et al. 2019). Nevertheless, in the early Universe, where merger rates are higher (Duncan et al. 2019; Duan et al. 2024a) and black hole growth is more intense, interactions may contribute to a significant amount of black hole growth. Indeed, large fractions of $z > 4.5$ AGN have companion galaxies or merger features (e.g., Duan et al. 2024b). Observations in the rest-frame far-infrared (FIR) with the Atacama Large Millimeter Array (ALMA) have detected companion galaxies around some high- z quasars at $\lesssim 60 \text{ kpc}$ separa-

* Email: mmarshall@lanl.gov

tions, interpreted as major galaxy interactions (e.g., Wagg et al. 2012; Decarli et al. 2017). In some high- z quasar samples, up to 50% have such companions (Trakhtenbrot et al. 2017). ALMA has also revealed gas bridges connecting quasar hosts and their nearby companions, clearly indicating ongoing interaction (e.g., Izumi et al. 2024; Zhu et al. 2024). Rest-frame UV observations have also discovered some kpc-scale companions around high- z quasars (McGreer et al. 2014; Farina et al. 2017; Marshall et al. 2020; Mazzucchelli et al. 2019), albeit less frequently than in the far-infrared (Willott et al. 2005), likely because many companion galaxies are dusty (Trakhtenbrot et al. 2017).

The local kpc-scale environments of high- z AGN are now being uncovered in the rest-frame UV and optical with JWST, with new insights due to its higher sensitivity and resolution combined with less dust attenuation in the optical. Many companion galaxies have been discovered within <10 kpc of $3 < z < 6$ AGN (Perna et al. 2023b,a; Matthee et al. 2024; Übler et al. 2023; Ji et al. 2024). Merger signatures have also been found around even higher-redshift AGN: $z \approx 7$ (Mérida et al. 2025), $z = 7.15$ (Übler et al. 2024b), and $z = 8.7$ (Larson et al. 2023). In the brighter ‘quasar’ regime, the previously discovered quasar–galaxy merger PSO J308.0416–21.2339 at $z \approx 6.2$ (Decarli et al. 2019) has been followed up with the JWST/NIRSpec integral field unit (IFU; Böker et al. 2022) to give detailed analysis of the gas and stellar emission from the system (Loiacono et al. 2024; Decarli et al. 2024). The NIRSpec IFU has also discovered that three quasars at $z = 6.8$ – 7.1 are undergoing mergers with nearby companion galaxies (Marshall et al. 2023, 2024). While companion galaxies and ongoing mergers are not ubiquitous, this growing sample suggests that mergers could be important for driving early black hole growth.

Mechtley (2014) and Marshall et al. (2020) observed six $z \approx 6$ quasars with deep HST/WFC3 IR imaging with the aim of detecting their host galaxies. To search for the light from the hosts, the quasar emission was modelled and subtracted via detailed subtraction techniques (Mechtley et al. 2012; Mechtley 2014, 2016). The subtracted images revealed numerous galaxies that had been hidden by the quasar emission. The J - and H -band colours and magnitudes of the neighbouring galaxies suggested that up to nine, surrounding five of the six quasars, could be potential $z \approx 6$ quasar companions (Marshall et al. 2020). These potential companions are separated from the quasars by $1''.4$ – $3''.2$ or projected 8.4–19.4 kpc if at the same redshift, and so may be interacting with the quasar hosts. The companions have UV absolute magnitudes of -22.1 to -19.9 and UV spectral slopes β of -2.0 to -0.2 , consistent with luminous star-forming galaxies at $z \approx 6$ (Bouwens et al. 2012; Dunlop et al. 2012; Finkelstein et al. 2012; Jiang et al. 2013, 2020). The Prime Extragalactic Areas for Reionization and Lensing Science (PEARLS) Guaranteed-Time Observation (GTO) program (Windhorst et al. 2023) has followed up two of these six $z \approx 6$ quasars with NIRSpec IFU observations. This paper presents the results for NDWFS J142516.3+325409, herein NDWFS J1425+3254. The data for the second quasar SDSS J000552.34–000655.8 will be presented elsewhere.

NDWFS J1425+3254 was discovered with the Hectospec spectrograph on the MMT, with a Lyman- α redshift of $z = 5.85$ (Cool et al. 2006). With the Plateau de Bure Interferometer (PdBI), CO (6–5) emission was detected at $z = 5.8918 \pm 0.0018$ (Wang et al. 2010). Shen et al. (2019) obtained rest-frame UV spectroscopy with GNIRS on Gemini-North, measuring a black hole mass from C IV of $(2.5^{+0.7}_{-0.6}) \times 10^9 M_{\odot}$, which combined with a bolometric luminosity of $(9.53 \pm 0.09) \times 10^{46}$ erg s $^{-1}$ corresponds to an Eddington ratio of $0.29^{+0.08}_{-0.06}$.

PEARLS targeted NDWFS J1425+3254 because it has two companion galaxies potentially at the redshift of the quasar (Mechtley 2014; Marshall et al. 2020). The Large Binocular Camera (LBC) on the Large Binocular Telescope (LBT) detected no g -band flux from these companions to $m_g \gtrsim 28.3$ mag (Marshall et al. 2020). In the r -band, there is only a constraint of $m_r \gtrsim 25.7$ mag for the companion furthest from the quasar on the sky (Mechtley 2014). The J - and H -band detections combined with faint g - and r -band limits exclude the possibility that these companions are blue foreground galaxies, but they could be red, luminous galaxies at $z \approx 1.1$. Further evidence for close companions comes from the Cool et al. (2006) spectrum, which has an absorption feature at ~ 8350 Å, ~ 20 Å red-ward of Lyman- α . This could come from H I absorption from a companion galaxy infalling at ~ 720 km s $^{-1}$ (Mechtley 2014). Thus the presence of close companions around NDWFS J1425+3254 seems likely, although requires spectroscopic confirmation.

This paper presents the NIRSpec IFU observations of NDWFS J1425+3254. Its goals are to confirm the redshift of the two potential companion galaxies to determine whether this is a merging system, study the ionised-gas properties of the host galaxy and the companions, and measure the quasar black hole mass and accretion rate. This paper is organized as follows. Section 2 describes the observations, data reduction, and analysis. Section 3 presents the quasar and black hole properties including the redshift, luminosity, black hole mass, and Eddington ratio. Section 4 focuses on the companion galaxies, presenting a range of properties including their star-formation rates, kinematics, and stellar masses. Section 5 presents a potential foreground lensing galaxy discovered in the data. In Section 6 we discuss our findings, and Section 7 gives an overall summary.

Throughout this work, we adopt the WMAP9 cosmology (Hinshaw et al. 2013) as included in ASTROPY (Astropy Collaboration et al. 2013) with $H_0 = 69.32$ km s $^{-1}$ Mpc $^{-1}$, $\Omega_M = 0.2865$, and $\Omega_{\Lambda} = 0.7134$. All quoted physical separations are proper distances. At the redshift of the quasar, $z = 5.89$, $1'' = 5.92$ kpc in this cosmology.

2. Observations and Data Analysis

2.1. JWST Observations

JWST observations of NDWFS J1425+3254 were taken as part of the PEARLS GTO program (PI R. Windhorst, PID #1176, Windhorst et al. 2023). The quasar was observed with the NIRSpec IFU in the prism/clear configuration, which gives spectral resolution $R \sim 100$ covering a wavelength range of 0.6–5.3 μ m. Wide-aperture target acquisition (WATA) was performed on the quasar to center the IFU at R.A. 14:25:16.4078, Decl. +32:54:09.580, slightly offset from the quasar position. This ensured that the extended neighbouring galaxies would be placed within the $3'' \times 3''$ field of view (FoV). The observations were taken on 2024 Feb 14, at a position angle of the telescope’s V3 axis of $271^\circ.6$.

The science observations consisted of two separate sets, both using the NRSIRS2RAPID readout pattern with 31 groups/integration, 1 integration, and a 4-point dither pattern to give 1867 s of exposure time. Combining the two sets gave a total science exposure time of 3735 s. Within the 4-point dither pattern, each dither has $0''.025$ sub-pixel offsets that improved the sampling of the point-spread function (PSF). One ‘leakcal’ observation set was also taken with observation specifications identical to the individual observation sets: a 4-point dither pattern with the same readout pattern and 1867 s total exposure time. The ‘leakcal’ was performed with the IFU aperture closed,

which measured spectral contamination from failed-open micro-shutter assembly (MSA) shutters. This leakcal was applied to both observation sets. The observations did not include separate background exposures because the sources are small enough to use blank areas within the FoV for background subtraction.

2.2. Data Reduction

To reduce the observations we used the JWST pipeline version 1.14.0 (Bushouse et al. 2022), with CRDS context file `JWST_1256.PMAP`. We followed the IFU reduction process provided by the TEMPLATES team (Rigby et al. 2023; Rigby et al. 2024) except for differences noted below. We included the snowball-masking jump-detection step, inbuilt into the JWST pipeline in Stage 1, to remove large cosmic-ray artefacts. We corrected $1/f$ noise using the NSClean package (Rauscher 2024). In Stage 2, we subtracted the leakcals from the science exposures dither-by-dither. This improves the quality of the final data cube, giving fewer spurious emission and absorption features; this improvement is more beneficial than the slight increase in background noise introduced by using the leakcals. We included the default pipeline outlier-detection step in Stage 3, which worked well for removing outliers in our data cube. To combine the data cubes, we used the *drizzle* algorithm and built the cube in sky coordinates. The output data cube has a pixel scale of $0''.05$, sub-sampled relative to the detector's $0''.1$ pixel scale, possible because of the dithering.

As the astrometry for the IFU is slightly uncertain, we assigned a new WCS based on the known quasar position from the Panoramic Survey Telescope & Rapid Response System (Pan-STARRS), which is astrometrically aligned to Gaia EDR3 (White et al. 2022). We found the peak, central sub-pixel quasar location via image smoothing and assigned this to the Pan-STARRS mean DR2 position, R.A. 14:25:16.3286, Decl. +32:54:09.554. This required only a simple shift by $\lesssim 0''.1$ with no rotation. Jones et al. (2024) gave a similar example with further details.

2.3. Analysis Technique

In this section we detail the techniques for our analysis of the data; the resulting measurements will be given and discussed in Sections 3 and 4.

2.3.1. Background and Continuum Subtraction

The first analysis step was to subtract the sky background from all spaxels in the data cube. The selected background region was a circular aperture of radius $0''.5$ near a corner of the IFU FoV, chosen to avoid the extended PSF of the quasar and emission from potential companions as well as the higher-noise pixels around the edge of the FoV. We defined the background spectrum as the median spectrum across spaxels within this aperture, which we then subtracted from each spaxel. Figure 1 shows the flux in this background-subtracted data cube integrated over $0.82\text{--}5.2\ \mu\text{m}$. We excluded the wavelengths from $0.6\text{--}0.82\ \mu\text{m}$, blue-ward of Lyman- α at $z = 5.8$, because they are dominated by noise.

To simplify fitting the emission lines, the focus of this work, we subtracted the continuum emission from the data cube. The continuum emission was based on flux densities in the emission-line- and iron-continuum-free windows at rest frame $1320\text{--}1330\ \text{\AA}$, $1455\text{--}1470\ \text{\AA}$, $1690\text{--}1700\ \text{\AA}$, $2160\text{--}2250\ \text{\AA}$, $3010\text{--}3040\ \text{\AA}$, $3240\text{--}3270\ \text{\AA}$, $3790\text{--}3810\ \text{\AA}$, $4180\text{--}4230\ \text{\AA}$, $5550\text{--}5630\ \text{\AA}$, and $5970\text{--}6000\ \text{\AA}$, based on the contin-

uum windows of Kuraszkiwicz et al. (2002) and Kovacevic et al. (2010), although slightly increasing the width of some of their windows to be more compatible with our low-resolution spectra. We also added two additional windows near the red edge of the spectral range at $7080\text{--}7130\ \text{\AA}$ and $7370\text{--}7630\ \text{\AA}$ to better constrain the red end of the rest-frame-optical continuum. We characterised the spaxels into three categories based on their median signal-to-noise ratio S/N in the continuum windows above $2.6\ \mu\text{m}$ —bright continuum with $S/N > 4.5$, intermediate continuum with $S/N > 3.5$, and faint continuum with $S/N > 1.5$. For the bright-continuum spaxels, we estimated the continuum level by cubic-spline interpolation between the median fluxes of each continuum window. For the intermediate-continuum spaxels, we used the cubic spline interpolation for $\lambda > 2.6\ \mu\text{m}$, and for $\lambda \leq 2.6\ \mu\text{m}$, we fit a quadratic to the continuum window medians at $\lambda < 3\ \mu\text{m}$ (with the overlap region in the polynomial fit helping to minimize the discontinuity at $\lambda = 2.6\ \mu\text{m}$). For the faint continuum, we used two quadratic fits: for $\lambda \leq 2.6\ \mu\text{m}$, a fit to the window medians at $\lambda < 3\ \mu\text{m}$, and for $\lambda > 2.6\ \mu\text{m}$, a fit to the window medians at $\lambda > 2.55\ \mu\text{m}$. We used quadratic fits for lower S/N spectra because the cubic interpolation can introduce artificial oscillations due to over-fitting of the data. We did not subtract the continuum in spaxels with $S/N < 1.5$; any remaining continuum is negligible and varies minimally with wavelength, and therefore does not affect the emission-line fitting. These continuum models were subtracted from the spectrum spaxel-by-spaxel to create a continuum-subtracted cube.

As found by Übler et al. (2023), Rodríguez Del Pino et al. (2024), Jones et al. (2024), and Lamperti et al. (2024), the noise estimation from the default ‘ERR’ cube output from the reduction pipeline underestimates the true noise seen in the data cube. Following the approach of those studies, we increased the ERR cube by a constant factor within each spaxel to match the observed noise. To estimate these multiplicative factors, we measured the root mean square (RMS) noise across the continuum windows of $5550\text{--}5630\ \text{\AA}$ and $5970\text{--}6000\ \text{\AA}$, the two windows between $H\beta$ and $H\alpha$, in the continuum-subtracted cube. In spaxels where the ratio of the RMS to the mean ERR in the same windows is greater than 1, we multiplied the ERR spectrum by RMS/ERR to give a more realistic estimation of the uncertainty in the data cube. The median multiplicative factor across the data cube is 1.55.

2.3.2. Quasar Spectral Fitting

To estimate the black hole properties, we perform model fitting on the integrated quasar spectrum around $H\beta$ and $H\alpha$. We integrated the background-subtracted cube across an aperture centred on the peak of the quasar emission. We chose the aperture radius to be the outer radius of the inner core of the PSF, just prior to the ring of reduced flux—this maximizes the quasar S/N while containing the majority of the quasar flux. This gives aperture radii of $0''.25$ for the spectrum around $H\beta$ at $\sim 3.4\ \mu\text{m}$, and $0''.35$ for the region around $H\alpha$ at $\sim 4.5\ \mu\text{m}$, from the PSFs we measure in Section 2.3.3 and Appendix A. To determine the appropriate aperture correction, we measure how much of the AGN broad-line flux is contained within this aperture, relative to that in the full PSF shape. We determine an aperture correction of $1.149 \times$ for $H\beta$, and $1.119 \times$ for $H\alpha$, that we apply to these integrated quasar spectra. Figure 2 shows the $0''.35$ aperture integrated spectrum.

Using this integrated spectrum, we perform model fitting using the code QUBESPEC¹, which models spectra via a Markov-chain Monte Carlo (MCMC) process. We fit each narrow emis-

¹ <https://github.com/honzaschoultz/Qubespec>

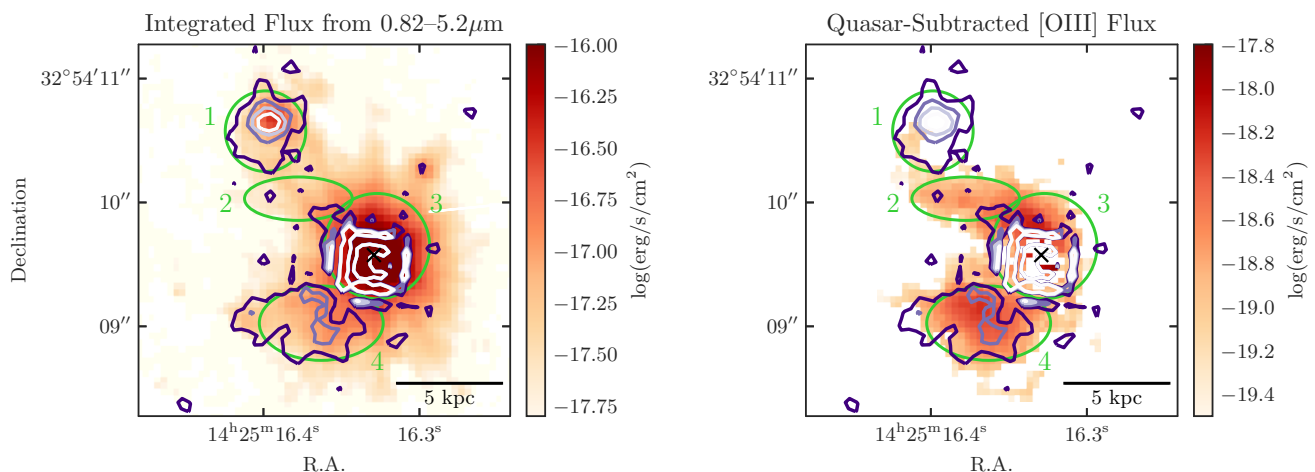


Fig. 1. *Left:* The flux from the full data cube integrated across 0.82–5.2 μm . *Right:* The [O III] $\lambda 5007$ flux map after quasar subtraction. Surface brightnesses are as indicated in the respective color bars. Purple to white contours show the quasar-subtracted HST/WFC3 F125W surface brightness (Marshall et al. 2020, who found very similar F160W morphology). Four regions are marked by the green elliptical apertures: Region 1 is the north-eastern companion galaxy, Region 2 is a bridge of connecting gas, the quasar host galaxy is Region 3, and Region 4 is the south-eastern companion galaxy. The maps are aligned along the cardinal directions, with north upwards and east to the left.

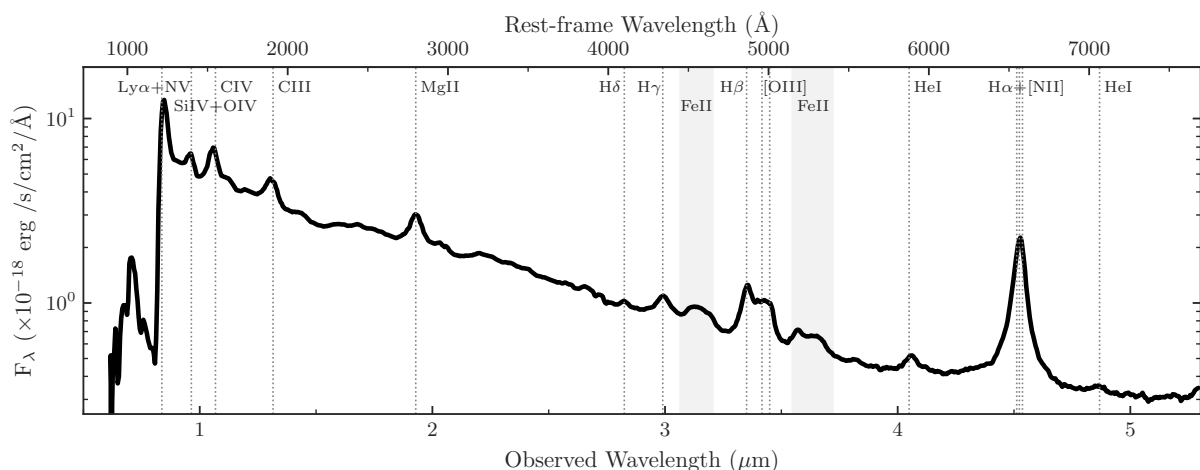


Fig. 2. The integrated quasar spectrum (black curve) showing the full wavelength range covered by the NIRSpec prism. The spectrum was measured within an aperture of radius $0''.35$ centred on the quasar emission peak, with an aperture correction of $1.119 \times$ applied. The green curve shows the 5σ uncertainty level of the spectrum. Key quasar and galaxy emission lines are marked with dotted vertical lines, and regions of strong Fe II emission, where the numerous transitions form a pseudo-continuum, are shaded.

sion line $H\beta$, [O III] $\lambda\lambda 4959, 5007$, $H\alpha$, and [N II] $\lambda\lambda 6548, 6584$, with two Gaussian components, one for the true ‘narrow’ galaxy emission, and one for a broader ‘outflow’ component. For the quasar broad line region (BLR), we fit the broad $H\beta$ and $H\alpha$ lines each with two Gaussians centred on the same redshift—a double Gaussian model—as has been used previously for high- z quasars observed with JWST (e.g., Yue et al. 2024; Marshall et al. 2024). This gives a better fit to the spectrum than a single Gaussian BLR model. We fit the continuum emission as a simple 1D power-law across the wavelength region of interest. We also included a template (Park et al. 2022) for the quasar Fe II emission.

The [O III] $\lambda\lambda 4959, 5007$ and [N II] $\lambda\lambda 6548, 6584$ doublet flux ratios were fixed to standard values, 2.98 for [O III] $\lambda 5007$ /[O III] $\lambda 4959$ (Storey & Zeppen 2000) and 3.05 for [N II] $\lambda 6584$ /[N II] $\lambda 6548$ (Dojčinović et al. 2023). Galaxy emission lines are expected to have $F_{H\alpha}/F_{H\beta} = 2.86$ for Case B recombination at a temperature $T = 10^4$ K and electron density $n_e = 10^2 \text{ cm}^{-3}$ (Osterbrock 1989). Dust attenuation and an AGN contribution would make the ratio larger than 2.86. We

therefore constrained the narrow, outflow, and two BLR $H\alpha$ line peak amplitudes to be between 2.5–10 times larger than those of $H\beta$, to aid the model in finding a physically realistic fit to the data; we chose the lower limit of 2.5 instead of 2.86 to account for uncertainties and systematic effects. The narrow and outflow $H\alpha$ and [N II] $\lambda\lambda 6548, 6584$ lines were constrained to have the same redshift and physical velocity width across all three emission lines, as we assume they arise from the same physical region with the same kinematics. We made the same assumption for the narrow and outflow $H\beta$ and [O III] $\lambda\lambda 4959, 5007$ lines. The Fe II emission was constrained to have the same redshift as the $H\beta$ BLR in the fit, given the low spectral resolution of our data (see Kovacevic et al. 2010, figure 16). We constrained the Fe II line width to have $\text{FWHM}_{\text{obs}} < 2100 \text{ km s}^{-1}$, as otherwise it becomes artificially large and gives a visually poorer fit.

The observed line width is a convolution of the physical velocity width of the line with the instrumental velocity width, such that $\text{FWHM}_{\text{obs}} = \sqrt{\text{FWHM}_{\text{phys}}^2 + \text{FWHM}_{\text{inst}}^2}$. The NIRSpec prism spectral resolution varies by a factor of ≥ 5 from

0.6 to $5.3 \mu\text{m}$. This results in a significantly larger $\text{FWHM}_{\text{inst}}$ at the wavelengths of $\text{H}\beta$ – $[\text{O III}] \lambda\lambda 4959, 5007$ than at $\text{H}\alpha$ – $[\text{N II}] \lambda\lambda 6548, 6584$, that must be accounted for. In Appendix B we present the line-spread function (LSF) for the NIRSpec IFU prism measured using observations of the planetary nebula SMP LMC 58. We measure the spectral resolution to be $\sim 14\%$ higher than the pre-flight expectations. From this LSF we can estimate that $\text{FWHM}_{\text{inst}, \text{H}\beta} = 2083 \pm 188 \text{ km s}^{-1}$ and $\text{FWHM}_{\text{inst}, \text{H}\alpha} = 1126 \pm 102 \text{ km s}^{-1}$. For our QUBESPEC fitting we use these two constant values across the $\text{H}\beta$ – $[\text{O III}]$ and $\text{H}\alpha$ – $[\text{N II}]$ wavelength regions respectively. The change in resolution across each wavelength range is $\lesssim 100 \text{ km s}^{-1}$, insignificant relative to the $\sim 200 \text{ km s}^{-1}$ uncertainty (see Section 2.3.4 and Appendix B).

We fit the two wavelength regions of $\text{H}\beta$ – $[\text{O III}]$ and $\text{H}\alpha$ – $[\text{N II}] \lambda\lambda 6548, 6584$ separately, due to the wavelength variation of the PSF warranting different integration apertures. However, as the emission lines arise from the same physical system, after first fitting the $\text{H}\beta$ – $[\text{O III}] \lambda\lambda 4959, 5007$ region, we used the resulting fit parameters in the priors for the $\text{H}\alpha$ – $[\text{N II}] \lambda\lambda 6548, 6584$ fit to ensure that the line velocities and velocity widths are generally consistent. In the $\text{H}\alpha$ – $[\text{N II}] \lambda\lambda 6548, 6584$ spectral fit, we defined the priors for the narrow, outflow, and two BLR line redshifts and widths to be normally distributed around the best-estimate redshifts and line widths from the $\text{H}\beta$ – $[\text{O III}] \lambda\lambda 4959, 5007$ fit, accounting for the instrumental resolution.

We ran the QUBESPEC MCMC for 80000 iterations. QUBESPEC uses 64 walkers with a burn-in of 25% of the iterations. The resulting model fit is shown in Figure 3. To determine the resulting emission line properties, we randomly chose 100 sets of model-parameter values from the output chain; we find that this adequately samples the full distribution. We then calculated the 16th, 50th, and 84th percentiles of the resulting line fluxes, luminosities, and FWHMs (Section 3).

2.3.3. Quasar Subtraction

Measuring the underlying emission from the host galaxy requires modelling and subtracting the quasar emission from the cube. The quasar emits both narrow emission lines from the narrow line region (NLR) and broad emission lines from the BLR, which is a spatially unresolved point source at this redshift. While the host galaxy also emits narrow emission lines through star formation, only the quasar BLR produces the broad emission features seen in quasar spectra. Thus a map of the BLR flux is a map of the quasar’s point-source emission, that is, the instrumental PSF. We can use this PSF to subtract both the quasar BLR and spatially-unresolved NLR emission from the data cube, to isolate the host galaxy emission.

Using the software QDeblend3D (Husemann et al. 2013, 2014), we use the BLR flux in each spaxel to determine the PSF shape. We measure the flux in the BLR line wings, to avoid the line centres where the narrow lines would contaminate the measurement. We measure these BLR fluxes for both the $\text{H}\beta$ and $\text{H}\alpha$ broad lines, as the PSF varies with wavelength. For $\text{H}\alpha$, we measure the flux across rest-frame 6485 – 6525 \AA and 6605 – 6640 \AA , either side of the emission peak at 6564.6 \AA . For $\text{H}\beta$, we measure the flux across rest-frame 4800 – 4850 \AA , on the blue side of the peak at 4862.68 \AA ; we only consider the blue wing due to the blending with $[\text{O III}] \lambda 4959$ on the red-ward side of the line. Figure A.1 shows the resulting 2D $\text{H}\alpha$ and $\text{H}\beta$ BLR flux maps, that is, the IFU PSF shape at 3.35 and $4.52 \mu\text{m}$.

We then take the spectrum from the central, brightest spaxel as our estimated quasar spectrum. This assumes the quasar flux is dominant and the host flux is negligible, a reasonable assumption across much of the spectral range given the non-detection of the host flux in the PSF-subtracted HST F125W and F160W images (Marshall et al. 2020). After scaling this quasar spectrum by the 2D PSF to create a quasar cube, we subtracted the quasar cube from the original continuum-subtracted data cube, resulting in a galaxy emission cube where the quasar contribution has been removed.

The quasar subtraction process adds additional uncertainty on the resulting data cube. To estimate this increase (following Marshall et al. 2023, 2024), we generated 200 realisations of the continuum-subtracted cube, applying normally distributed noise from our rescaled ‘ERR’ array and performing the same quasar subtraction on each realisation. We calculate the standard deviation across the resulting 200 host galaxy cubes at each wavelength in each spaxel. We determine the ratio of the mean standard deviation around the peaks of $\text{H}\alpha$ and $\text{H}\beta$ within rest-frame 25 \AA to the same measurement on the original host cube, and multiply the rescaled the ‘ERR’ array by these fractions. The maximum uncertainty increase around $\text{H}\beta$ was a factor of 2.17, and the maximum around $\text{H}\alpha$ was a factor of 3.02.

Because we performed the quasar subtraction separately for $\text{H}\beta$ and $\text{H}\alpha$, we used the $\text{H}\beta$ subtracted data cube and ERR cube for $\lambda \leq 4 \mu\text{m}$, and the $\text{H}\alpha$ subtracted data cube and ERR cube for $\lambda > 4 \mu\text{m}$. However, the PSF varies significantly with wavelength. This paper considers only lines in the immediate vicinity of $\text{H}\beta$ and $\text{H}\alpha$, where no significant PSF-variation effects are expected. At wavelengths away from these lines, the quasar-subtracted data will be inaccurate, and a different method of quasar subtraction would be required.

2.3.4. Host Line Fitting

We map the extended emission within both the full (non-quasar subtracted) and quasar-subtracted (host galaxy) data cubes, to visualise the effect of the quasar subtraction. We only consider the emission lines immediately surrounding $\text{H}\beta$ and $\text{H}\alpha$, as the quasar subtraction is only reliable at these wavelengths.

We modelled the emission lines at each spatial position with Gaussian functions. The quasar also produces Fe II emission, which we modelled using an iron emission template from Park et al. (2022) in the full data cube. For spaxels in the full data cube where the mean S/N across rest-frame 5150 – 5370 \AA (in the Fe II emission region) is greater than 2, we fit the ‘quasar spectral model’, which models the $\text{H}\alpha$ and $\text{H}\beta$ lines with two separate Gaussian components, one for the narrow galactic emission and a broader component for the BLR emission, the $[\text{O III}] \lambda\lambda 4959, 5007$ and $[\text{N II}] \lambda\lambda 6548, 6584$ lines as single narrow Gaussians, and includes the Park et al. (2022) Fe II template. In other spaxels in the full (non-quasar-subtracted) cube and in all spaxels within the quasar-subtracted cube, we fit a single narrow Gaussian function for each of $\text{H}\beta$, $[\text{O III}] \lambda\lambda 4959, 5007$, $[\text{N II}] \lambda\lambda 6548, 6584$, and $\text{H}\alpha$. These fits included no Fe II .

The fits constrained the $[\text{O III}] \lambda\lambda 4959, 5007$ and $[\text{N II}] \lambda\lambda 6548, 6584$ doublet flux ratios to 2.98 for $[\text{O III}] \lambda 5007 / [\text{O III}] \lambda 4959$ and 3.05 for $[\text{N II}] \lambda 6584 / [\text{N II}] \lambda 6548$. We constrained all of the narrow lines to have the same central velocity and physical width, $\text{FWHM}_{\text{phys}}$. In Appendix B, we measure instrumental velocity widths of $\text{FWHM}_{\text{inst}} = 2083 \pm 188 \text{ km s}^{-1}$, $1997 \pm 181 \text{ km s}^{-1}$, $1966 \pm 178 \text{ km s}^{-1}$, and $1126 \pm 102 \text{ km s}^{-1}$, at the wavelengths

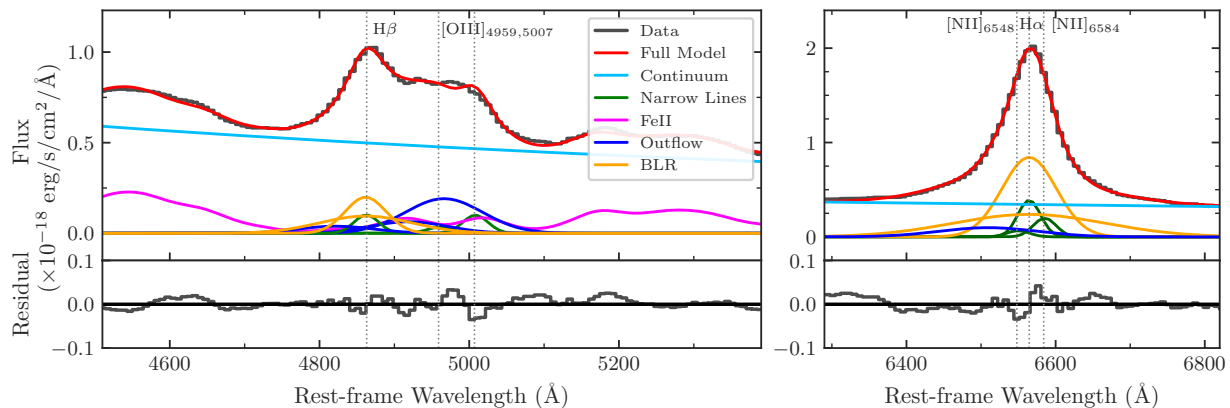


Fig. 3. The integrated quasar spectrum in an aperture centred on the peak of the quasar emission. *Left:* The region around $H\beta$ – $[O\text{ III}]$ with an aperture radius of $0''.25$. *Right:* the region around $H\alpha$ – $[N\text{ II}]$ with an aperture radius of $0''.35$. The solid black in the upper panel shows the observations, and the red line shows the best model fit from QUBESPEC. The individual components of the model fit are also shown as indicated in the legend: the power-law continuum emission, Gaussian narrow and outflow lines, double-Gaussian BLR model, and Park et al. (2022) Fe II template. The lower panels show the residual between the observed flux and the full model. No aperture correction has been applied to this figure, but an aperture correction of $1.119\times$ for $H\alpha$ and $1.149\times$ for $H\beta$ was applied to all calculations from these spectral fits.

of $H\beta$, $[O\text{ III}]\lambda\lambda 4959, 5007$, and $H\alpha$ respectively, assuming that $\text{FWHM}_{\text{inst}, [\text{NII}]} = \text{FWHM}_{\text{inst}, H\alpha}$. We correct the observed FWHM_{obs} using these $\text{FWHM}_{\text{inst}}$ to constrain each line fit to have the same $\text{FWHM}_{\text{phys}}$. The broad $H\beta$ and $H\alpha$ components were similarly constrained to have the same central velocity and physical velocity width as each other (but different than the narrow lines).

To produce line maps, the line velocity and width were measured from the Gaussian fit to the lines in each spaxel. The velocity was measured as the Gaussian line peak relative to the quasar host redshift of $z = 5.901$. We corrected the measured Gaussian FWHMs for the instrumental resolution, that is, the maps depict $\text{FWHM}_{\text{phys}}$. The maps include spaxels where the emission line $S/N > 3$ and also adjacent spaxels with $S/N > 1.5$, following the `FIND_SIGNAL_IN_CUBE` algorithm of Sun (2020).

Figure 1 shows the $[O\text{ III}]\lambda 5007$ flux map after quasar subtraction. The quasar-subtracted HST/WFC3 F125W image from Marshall et al. (2020) is overlaid for comparison, with the F160W image showing very similar morphology. The integrated 0.82 – $5.2\mu\text{m}$ flux map, $[O\text{ III}]\lambda 5007$ flux map, and HST images show four clear structures in this system, depicted by the ellipses in Figure 1 and labelled Regions 1–4 from north to south. Region 1 lies to the north-east of the quasar, where faint $[O\text{ III}]\lambda 5007$ emission is coincident with bright integrated flux. Region 2 is an area of $[O\text{ III}]\lambda 5007$ emission between Region 1 and the quasar host galaxy (Region 3), that was not detected in the F125W or F160W HST imaging. Region 4 lies south-east of the quasar, emitting both bright $[O\text{ III}]\lambda 5007$ and continuum flux. Section 4 discusses these regions in detail.

2.3.5. Stellar Population Modelling

The emission-line maps reveal multiple emission-line regions surrounding the quasar (Figure 1; discussion in Section 4). To estimate the stellar properties of these regions, we performed simultaneous line and continuum fitting with pPXF (Cappellari & Emsellem 2004; Cappellari 2017, 2023), a penalised pixel-fitting algorithm. pPXF estimates the stellar-population properties via stellar population synthesis (SPS) modelling of the spectrum. We do not use the emission-line properties as fit by pPXF, instead favouring those from the continuum- and quasar-subtracted line

fitting reported in Section 2.3.4. We only report pPXF results for the stellar population properties.

For pPXF to model the stellar population, it must be supplied with input spectra that include the continuum emission. We therefore cannot use the quasar-subtracted data cubes, which are first continuum subtracted (Section 2.3.3). The significant PSF variation with wavelength makes it impossible to accurately subtract the quasar emission across the full wavelength range, outside of the immediate area of $H\beta$ and $H\alpha$, using the quasar-subtraction methods used here. Therefore we cannot create quasar-subtracted cubes that accurately depict the continuum emission. Instead, we use the original data cube and select only spatial regions that include negligible quasar flux. As the Region 2 and 4 apertures used throughout the rest of this work overlap the quasar $H\beta$ and $H\alpha$ PSF shapes, thus containing significant quasar flux, we defined two smaller elliptical aperture regions (Regions 2* and 4*, Figure A.1) that avoid such overlap. Regions 2* and 4* do not contain all of the flux from the respective sources, but they show the uncontaminated continuum shape and thus allow for modelling of the stellar populations. We therefore integrated the spectra within the Region 1, 2*, and 4* apertures (Figure A.1) to obtain a spectrum for each region. The continuum flux in Region 2* is very faint with typical $S/N \lesssim 5$. To allow a measurement of the continuum in this region, we rebinned its spectrum onto a $10\times$ -coarser wavelength grid. Region 3, the host galaxy, is hidden behind the quasar emission and cannot be modelled with the methods used here.

The pPXF modelling of Regions 1, 2*, and 4* followed a method similar to that of Cameron et al. (2023) and the pPXF examples.² We used the SPS templates from the flexible SPS (FSPS) model (Conroy et al. 2009; Conroy & Gunn 2010, version 3.2) and a Salpeter (1955) initial mass function (IMF). We restricted the age of the templates to the age of the Universe at $z = 5.89$, 967 Myr. We adopted the dust attenuation law from Calzetti et al. (2000) and constrained the dust attenuation to be $0 \leq A_V \leq 1.5$ mag. For the emission lines, we fit a series of single Gaussian functions. We divided the emission lines into three groups, with lines in each group constrained to have the same radial velocity and width: hydrogen Balmer lines, UV lines

² https://github.com/micappe/ppxf_examples

($\lambda_{\text{rest}} < 3000 \text{ \AA}$), and optical lines ($\lambda_{\text{rest}} > 3000 \text{ \AA}$). The stellar component was free to have its own velocity and line width. To account for the instrumental line width, the templates were smoothed by the instrumental LSF (Appendix B). The measured flux blue-ward of Lyman-alpha was set to zero to assist with the fitting.

To estimate the uncertainties on the output properties, we performed bootstrapping following Kacharov et al. (2018) and using 100 samples. Our quoted values and uncertainties are the median, 16th, and 84th percentile values from these 100 samples. The output distributions of $[M/H]$ are not centrally peaked but instead cover a wide range of values and typically peak at one of the edges of the allowed parameter range. In these cases, we quote the minimum or maximum value from the 100 samples as a lower or upper limit. All reported stellar-population parameters are flux-weighted values.

3. Quasar and Black Hole Properties

Figure 2 shows the full integrated quasar spectrum from 0.6–5.3 μm . The spectrum has $S/N > 5$ between the Lyman limit at rest-frame 912 \AA and Lyman- α at 1216 \AA but no significant flux blue-ward of the Lyman limit. The spectrum has $S/N > 150$ between Lyman- α and 5 μm observed (rest 1216 $< \lambda < 7250 \text{ \AA}$). There are clear detections of the expected AGN emission lines, from Lyman- α to H α . S II is not detected. While N II is likely present, it is blended with the H α line and therefore difficult to decompose.

Figure 3 shows our best-fitting quasar spectral model around H β –[O III] $\lambda\lambda 4959, 5007$ and H α –[N II] $\lambda\lambda 6548, 6584$ from QUBESPEC. This model describes both regions well, with low residuals across the wavelength region. However, at this low spectral resolution the emission lines and their various kinematic components are blended together, and so precise modelling and line decomposition is limited. Higher spectral resolution data would allow for a more accurate modeling of the quasar.

3.1. Redshift and luminosity

We present our redshift measurements in Table 1. The MCMC fits gave a quasar redshift $z = 5.890 \pm 0.010$ from the NLR and $z = 5.888 \pm 0.010$ from the BLR. From the integrated quasar-subtracted spectrum, the host galaxy (Region 3) has a redshift $z = 5.901 \pm 0.010$ from the kinematically-tied H β , [O III], H α , and [N II] $\lambda\lambda 6548, 6584$ emission lines. The host galaxy redshift is the most relevant for tracing the kinematics throughout the system, which is a focus of this work. Therefore, we adopted the quasar host redshift $z = 5.901 \pm 0.010$ as the baseline redshift for all relative velocity calculations throughout this work.

Our redshift estimates are larger than the original redshift estimate from the break in the Lyman- α profile, $z = 5.85$ (Cool et al. 2006), as well as those from Shen et al. (2019), listed in Table 1. These rest-frame UV emission lines can have velocity offsets up to $\sim 1000 \text{ km s}^{-1}$ from the systemic redshift due to strong internal motions or winds in the BLR (e.g., Eilers et al. 2020), that may explain this discrepancy. In contrast, our redshift measurement is consistent with the CO redshift of $z = 5.8918 \pm 0.0018$ (Wang et al. 2010), which is a significantly more reliable indicator of the systemic velocity.

We calculated the integrated flux and FWHM of the broad-line components of H α and H β using 100 randomly selected sets of spectral model parameter values from the MCMC output chain. We measured a H α BLR luminosity of $42.9_{-0.1}^{+0.1} \times 10^{43} \text{ erg s}^{-1}$,

Table 1. Redshift measurements

Measurement	z	Unc.	Reference
Quasar and host galaxy			
Lyman- α	5.85	0.02	Cool et al. (2006)
CO	5.8918	0.0018	Wang et al. (2010)
C III]	5.861	0.007	Shen et al. (2019)
C IV	5.851	0.010	Shen et al. (2019)
Si IV	5.865	0.015	Shen et al. (2019)
Quasar NLR	5.890	0.010	This work
Quasar BLR	5.888	0.010	This work
Host galaxy	5.901	0.010	This work
Companions			
NE (Region 1)	5.882 ^a	0.010	This work
Bridge (Region 2)	5.891 ^a	0.010	This work
SE (Region 4)	5.902 ^a	0.010	This work
Possible lensing galaxy			
[O III], H α	1.135	0.010	This work

Notes. The quasar redshifts from this work are from the H β line for the BLR, and from the kinematically-tied [O III] $\lambda\lambda 4959, 5007$ and H β lines for the NLR. The host galaxy and companion redshifts are based on fits to the [O III] $\lambda\lambda 4959, 5007$, H β , [N II] $\lambda\lambda 6548, 6584$, and H α narrow lines, that are all kinematically tied to have the same redshift.

(^a) Redshift measurements of these regions with the cross-correlation program XCSAO (Kurtz & Mink 1998, spiral template covering rest wavelengths 2984 to 7379 \AA) were consistent with the tabulated values. When emission lines were excluded from the fit, the S/N of absorption features was too low to give a redshift measurement.

with line width $\text{FWHM}_{\text{phys}} = 4132_{-176}^{+194} \text{ km s}^{-1}$, and a H β BLR luminosity of $8.9_{-0.2}^{+0.3} \times 10^{43} \text{ erg s}^{-1}$, with line width $\text{FWHM}_{\text{phys}} = 3971_{-440}^{+363} \text{ km s}^{-1}$. The flux ratio $F_{\text{BLR,H}\alpha}/F_{\text{BLR,H}\beta} = 4.8 \pm 0.1$ is larger than that for a sample of blue AGN that are free of dust extinction (Dong et al. 2008), $F_{\text{BLR,H}\alpha}/F_{\text{BLR,H}\beta} = 3.06_{-0.33}^{+0.38}$, suggesting that NDWFS J1425+3254 has some dust attenuation of the BLR. We find a consistent amount of dust attenuation when measuring the H γ to H β flux ratio. However, because the intrinsic ratio $F_{\text{BLR,H}\alpha}/F_{\text{BLR,H}\beta}$ varies among AGN, we cannot precisely estimate the dust attenuation for single sources, only for statistical AGN samples (Dong et al. 2008), and so we do not correct the BLR properties for dust attenuation.

We measured the 5100 \AA rest-frame continuum flux as $(5.66 \pm 0.03) \times 10^{-19} \text{ erg s}^{-1} \text{ cm}^{-2} \text{ \AA}^{-1}$, from the mean of the flux between 5090–5110 \AA . To estimate the bolometric luminosity L_{bol} , we used the 5100 \AA bolometric correction of Runnoe et al. (2012b,a), $L_{\text{bol}} \simeq 0.75 L_{\text{iso}}$, with $\log(L_{\text{iso}}) = (1.017 \pm 0.001) \log(5100 L_{5100}) - (0.088 \pm 0.034) \alpha_{\lambda, \text{opt}}$. Here $\alpha_{\lambda, \text{opt}}$ is the optical slope such that $F_{\lambda} \propto \lambda^{\alpha_{\lambda, \text{opt}}}$. We fit our integrated spectrum across the region between rest-frame 3981 \AA and 6310 \AA , avoiding the Fe II emission and H β and [O III] $\lambda\lambda 4959, 5007$ emission lines, and measured an optical slope $\alpha_{\lambda, \text{opt}} = -2.24$. From this, we derived a bolometric luminosity of $L_{\text{bol}} = (5.7_{-1.0}^{+1.3}) \times 10^{46} \text{ erg s}^{-1}$ for NDWFS J1425+3254. This is lower than the Shen et al. (2019) estimate of $L_{\text{bol}} = (9.53 \pm 0.09) \times 10^{46} \text{ erg s}^{-1}$ based on the 3000 \AA luminosity, although they are consistent within 3σ .

3.2. Black hole mass

To estimate the black hole mass of NDWFS J1425+3254, we use single-epoch mass-scaling relations, which follow the form:

$$M_{\text{BH}} = a \left(\frac{L}{L_{\odot}} \right)^b \left(\frac{\text{FWHM}}{10^3 \text{ km s}^{-1}} \right)^c M_{\odot}, \quad (1)$$

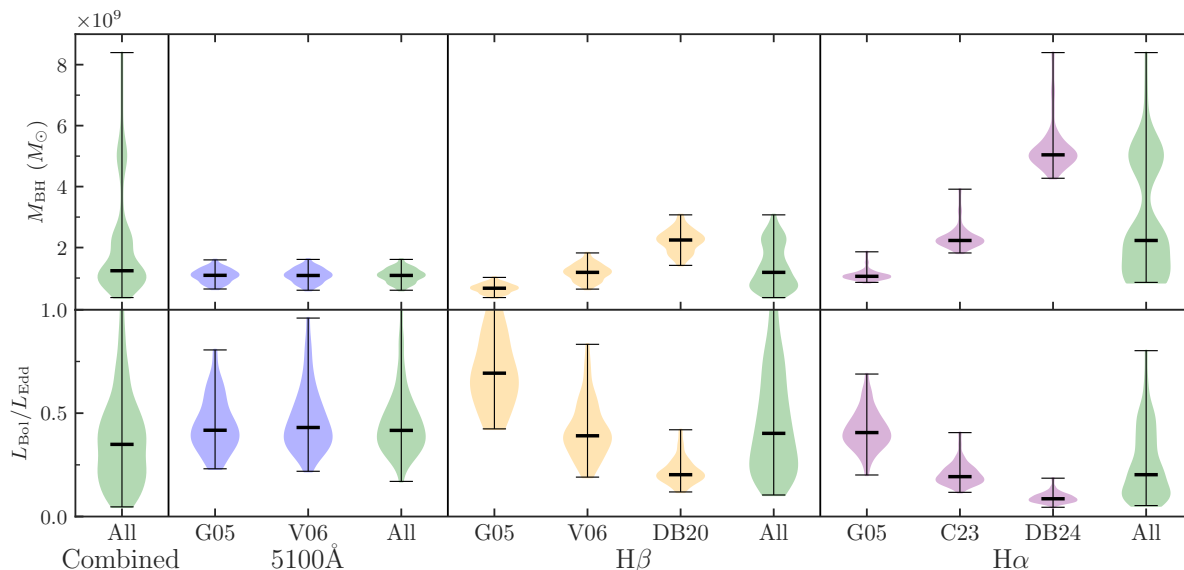


Fig. 4. Black hole mass and Eddington ratio estimates for NDWFS J1425+3254 from single-epoch mass-scaling relations (Equation 1), using the 5100 Å continuum luminosity and H β line FWHM (blue), the H β line luminosity and FWHM (yellow), the H α line luminosity and FWHM (purple). We show estimates using various calibrations to these relations, from Greene & Ho (2005, G05), Vestergaard & Peterson (2006, V06), Dalla Bontà et al. (2020, DB20), Dalla Bontà et al. (2024, DB24) and Cho et al. (2023, C23). The green curves show the combined probability distributions across each of the calibrations from each equation, and from all equations combined (left-most), assuming that each calibration and equation has equal weighting. The horizontal black lines mark the minimum, median, and maximum for each distribution. The probability distribution reflects the posterior distribution from the MCMC fit, that is, only the uncertainty in the fitting parameters is included, and not the ~ 0.4 dex scatter from the scaling relation conversion to a black hole mass. The top panel shows the black hole mass estimate, and the bottom panel shows the resulting Eddington ratio.

where the constants a , b , and c are calibrated from reverberation mapping studies at low- z to measurements of the luminosity and FWHM of quasar BLR emission lines as well as their continuum luminosity (e.g., Wandel et al. 1999; Kaspi et al. 2000). We considered three different scaling relation types from the literature, using the 5100 Å continuum luminosity and the luminosity L and line FWHM from the H β and H α BLR lines as follows.

5100 Å–H β relation: These equations use the 5100 Å continuum luminosity, making $L/L_0 = \lambda L_{5100}/10^{44} \text{ erg s}^{-1}$, and the FWHM of the H β BLR line component. These relations set $c = 2$. Greene & Ho (2005) calibrated the other constants to be $a = (4.4 \pm 0.2) \times 10^6$, $b = 0.64 \pm 0.02$, whereas Vestergaard & Peterson (2006) derived $a = (8.1 \pm 0.4) \times 10^6$, $b = 0.50 \pm 0.06$. **Pure H β relation:** To avoid the difficulty in measuring the continuum luminosity, these equations use the line luminosity of the H β BLR line component, making $L/L_0 = L_{H\beta}/10^{42} \text{ erg s}^{-1}$, and the H β FWHM. Greene & Ho (2005) set $c = 2$ and derived $a = (3.6 \pm 0.2) \times 10^6$, $b = 0.56 \pm 0.02$. Vestergaard & Peterson (2006), also with $c = 2$, derived $a = (4.7 \pm 0.3) \times 10^6$, $b = 0.63 \pm 0.06$. Dalla Bontà et al. (2020) found $a = 10.1 \times 10^6$, $b = 0.784$, and $c = 1.387$.

Pure H α relation: Similar to the pure H β relations, these equations use the line luminosity of the H α BLR line component, such that $L/L_0 = L_{H\alpha}/10^{42} \text{ erg s}^{-1}$, and the H α FWHM. From Greene & Ho (2005), $a = 2.0^{+0.4}_{-0.3} \times 10^6$, $b = 0.55 \pm 0.02$, and $c = 2.06 \pm 0.06$. Cho et al. (2023) found $a = (3.20 \pm 0.3) \times 10^6$, $b = 0.61 \pm 0.04$, with $c = 2$. Dalla Bontà et al. (2024) found $a = 3.58 \times 10^6$, $b = 0.812$, and $c = 1.634$.

Using our measured H β and H α broad line properties, we calculated the black hole masses using Equation 1, for each of the three scaling relation types and each of the quoted calibrations, for the 100 sets of spectral model parameter values. Figure 4

shows the distributions of black hole masses for each calibration of each scaling relation. The figure also shows the various calibrations combined, assuming an equal weighting. Combining all of the scaling relations and calibrations together gives $M_{\text{BH}} = (1.2^{+1.3}_{-0.4}) \times 10^9 M_{\odot}$, but this estimate does not take into account that each scaling relation has an intrinsic uncertainty of ~ 0.4 dex (Vestergaard & Peterson 2006; Dalla Bontà et al. 2020, 2024). To allow for that, we applied 1000 realisations of 0.4 dex noise to the black hole masses calculated from the 100 sets of model parameter values for each scaling relation. As these measurements have non-Gaussian distributions, this is more robust than simply adding the uncertainties in quadrature. This gives $M_{\text{BH}} = (1.1^{+1.6}_{-0.6}) \times 10^9 M_{\odot}$ for the 5100 Å–H β relation, $M_{\text{BH}} = (1.2^{+2.3}_{-0.8}) \times 10^9 M_{\odot}$ for the pure H β relation, and $M_{\text{BH}} = (2.3^{+4.9}_{-1.6}) \times 10^9 M_{\odot}$ for the pure H α relation. While the different methods produce different mass estimates, all estimates are consistent within the large uncertainties. Combining all three scaling relations and their uncertainties gives $M_{\text{BH}} = (1.4^{+3.1}_{-1.0}) \times 10^9 M_{\odot}$. This is consistent with the black hole mass estimate of $(2.5^{+0.7}_{-0.6}) \times 10^9 M_{\odot}$ from C iv (Shen et al. 2019, whose uncertainties do not account for the intrinsic scatter in the scaling relations).

3.3. Eddington ratio

The Eddington luminosity can be estimated as

$$L_{\text{Edd}} = \frac{4\pi G m_p c M_{\text{BH}}}{\sigma_{\text{T}}} = 1.26 \times 10^{38} \left(\frac{M_{\text{BH}}}{M_{\odot}} \right) \text{ erg s}^{-1}, \quad (2)$$

where G is the gravitational constant, m_p the proton mass, c the speed of light, and σ_{T} the Thomson scattering cross-section. We calculated the Eddington ratio $L_{\text{Bol}}/L_{\text{Edd}}$ using each of our black

hole mass estimates, and Figure 4 shows the results. Combining all of the scaling relations and calibrations together gives $L_{\text{Bol}}/L_{\text{Edd}} = 0.35^{+0.22}_{-0.20}$, consistent with the Shen et al. (2019) measurement of $0.29^{+0.08}_{-0.06}$ from C iv. These uncertainties consider only measurement uncertainties, and not the 0.4 dex intrinsic scatter in the black hole mass scaling relations. Adding that scatter gives $L_{\text{Bol}}/L_{\text{Edd}} = 0.3^{+0.6}_{-0.2}$. NDWFS J1425+3254 is most likely accreting at a sub-Eddington rate typical of quasars at both low- and high- z (Shen et al. 2011, 2019; Farina et al. 2022) but much higher than for local radio galaxies (e.g., Stasińska et al. 2025).

3.4. Outflow

There is a clear detection of an outflow signature from the integrated quasar spectrum in Figure 3, as traced by a broad kinematic component in [O III] $\lambda\lambda 4959, 5007, \text{H}\beta$, and $\text{H}\alpha$. These outflows have a total luminosity of $(7.9^{+0.2}_{-0.5}) \times 10^{43} \text{ erg s}^{-1}$, $(1.6^{+0.1}_{-1.2}) \times 10^{43} \text{ erg s}^{-1}$, and $(5.2 \pm 0.1) \times 10^{43} \text{ erg s}^{-1}$ in [O III] $\lambda 5007, \text{H}\beta$, and $\text{H}\alpha$ respectively. The [O III] $\lambda 5007$ outflow component has a line width of $\text{FWHM}_{\text{phys}} = 7080^{+238}_{-1186} \text{ km s}^{-1}$, with a velocity offset of $-2510^{+450}_{-220} \text{ km s}^{-1}$ relative to the narrow Gaussian component, with $\text{H}\alpha$ and $\text{H}\beta$ tied to have consistent line widths and velocities. This corresponds to an outflow velocity $v_{\text{out}} = v_{\text{offset}} + \text{FWHM}/2 = 6050^{+460}_{-630} \text{ km s}^{-1}$. This high-speed outflow is comparable to those of the most extreme quasar-driven outflows in the Universe (e.g. Perrotta et al. 2019; Zamora et al. 2024; Vayner et al. 2024).

While this outflow is extreme, it provides the best explanation for the relatively flat spectrum between rest-frame 4900–5000Å. If no outflow component is included in the spectral model, large residuals are present around [O III] $\lambda 4959$, with this wavelength region significantly under fit. There may be some contribution in this region from other transitions such as He I (as in e.g. Übler et al. 2023), that cannot be excluded because of the low spectral resolution. The Fe II template may also not be an ideal model for this quasar. However, neither explanation is likely to account for the significant flux around [O III] $\lambda 4959$, and so these broad outflows are the most likely scenario. This $\text{H}\beta$ –[O III] $\lambda\lambda 4959, 5007$ spectral shape is very similar to that of the $z \approx 2$ extremely red quasar J102541.78+245424.2, with relatively constant flux between rest-frame 4900–5000Å, that was measured to have a similar extreme outflow with [O III] $\lambda 4959$ FWHM of $5751 \pm 195 \text{ km s}^{-1}$ (Perrotta et al. 2019), further supporting this outflow scenario.

Following Carniani et al. (2015), we calculate the outflow masses from the [O III] $\lambda 5007$ and $\text{H}\beta$ luminosities, assuming a density of the gas in the ionised outflow of $\langle n_e \rangle = 500 \text{ cm}^{-3}$, measuring $M_{\text{out,H}\beta} = (27^{+1}_{-20}) \times 10^7 M_{\odot}$ and $M_{\text{out,[OIII]}} = (6.3^{+0.1}_{-0.4}) \times 10^7 M_{\odot}$. From the [O III] $\lambda 5007$ FWHM maps in Figure 5, this broad emission is not present after PSF subtraction, implying that it is spatially unresolved. We therefore assume an outflow radius $R_{\text{out}} = 1 \pm 0.1 \text{ kpc}$, approximately the spatial resolution of JWST, as in Zamora et al. (2024). We estimate the ionised outflow rate $\dot{M}_{\text{out}} = M_{\text{out}} v_{\text{out}} / R_{\text{out}}$ as $1650^{+130}_{-1230} M_{\odot} \text{ yr}^{-1}$ from $\text{H}\beta$ and $393^{+31}_{-50} M_{\odot} \text{ yr}^{-1}$ from [O III] $\lambda 5007$. The kinetic power of the outflows can be estimated as $\dot{P}_{\text{K,out}} = \frac{1}{2} \dot{M}_{\text{out}} v_{\text{out}}^2$, corresponding to $(19^{+3}_{-14}) \times 10^{45} M_{\odot} \text{ erg s}^{-1}$ from $\text{H}\beta$ and $(4.5^{+0.6}_{-0.9}) \times 10^{45} \text{ erg s}^{-1}$ from [O III] $\lambda 5007$. These are $33^{+5}_{-25} \%$ and $8 \pm 1 \%$ of the bolometric luminosity of the quasar, implying very powerful outflows.

These measurements suggest that NDWFS J1425+3254 has a very powerful quasar-driven ionised gas outflow, potentially one

of the most extreme in the early Universe. This outflow would likely quench the star formation in the host galaxy, with very large outflow rates and kinetic power. However, these measurements rely on the model fit to the low resolution spectral data, in which the various emission line components are highly blended. More accurately constraining these outflow properties and confirming its extreme nature requires higher spectral resolution data, and so we present this only as tentative evidence of such an extreme outflow.

4. Extended Emission Structures

4.1. Spectroscopic confirmation of two companion galaxies and discovery of a gas bridge

Figure 5 shows the [O III] $\lambda 5007$ flux and velocity maps for the system, both before and after subtracting the quasar’s contribution. The brightest region of [O III] $\lambda 5007$ is emitted from the quasar, following the PSF shape, with line FWHM $\gtrsim 4000 \text{ km s}^{-1}$. There are also extended regions of [O III] $\lambda 5007$ emission in the south and northwest, which are extended beyond the PSF shape and are clearly seen even before quasar subtraction. After quasar subtraction, some [O III] $\lambda 5007$ emission is also seen from the quasar host galaxy, although this is difficult to detect relative to the bright quasar emission. Despite the quasar subtraction resulting in a core of artefacts in the close vicinity of the quasar, it gives a much clearer picture of the kinematics of the extended emission line regions.

Figure 1 shows the [O III] $\lambda 5007$ flux distribution after quasar subtraction, alongside the integrated 0.82–5.2 μm flux map and the quasar-subtracted HST/WFC3 F125W image (Marshall et al. 2020). The north-east corner of the data cube exhibits faint [O III] $\lambda 5007$ emission coincident with a bright region of continuum emission. From the WFC3 F125W and F160W imaging of this north-eastern source, Marshall et al. (2020) measured $m_J = 24.6 \pm 0.1 \text{ mag}$ and $m_J - m_H = 0.4 \pm 0.1 \text{ mag}$. This corresponds to a UV absolute magnitude $M_{1500} = -21.8 \pm 0.2 \text{ mag}$ and UV slope $\beta = -0.4 \pm 0.8$, assuming the source is at the same redshift as the quasar. Marshall et al. (2020) fit the source with a Sérsic profile, finding a best-fitting index of $n = 3.6 \pm 0.7$, radius $R_e = 2.6 \pm 0.4 \text{ kpc}$, and axis ratio $b/a = 0.81 \pm 0.21$, at a projected distance of $\sim 1''.4$ or $8.4 \pm 0.1 \text{ kpc}$ from the quasar. Based on the UV slope and magnitude, Marshall et al. (2020) concluded that this source was likely a high- z galaxy, not a foreground interloper. Our IFU spectra confirm that this source is indeed a companion galaxy at the same redshift as the quasar.

Figure 1 shows a region of [O III] $\lambda 5007$ emission connecting the quasar host galaxy and the north-east companion. This “Region 2” has much larger [O III] $\lambda 5007$ flux than Region 1, yet no continuum emission from this region is detected in the F125W or F160W HST imaging. The lack of continuum detection suggests that Region 2 is most likely a connecting bridge of hot, ionised gas between the host galaxy and the north-eastern companion.

To the south-east of the quasar, Marshall et al. (2020) discovered a bright galaxy in the F125W and F160W imaging, with $m_J = 24.4 \pm 0.1 \text{ mag}$ and $m_J - m_H = 0.1 \pm 0.1 \text{ mag}$. This corresponds to UV magnitude $M_{1500} = -22.3 \pm 0.2 \text{ mag}$ and UV slope $\beta = -1.6 \pm 0.6$. The HST imaging for this companion is best fit with a Sérsic profile with index of $n = 0.5 \pm 0.1$, radius $R_e = 2.7 \pm 0.1 \text{ kpc}$, and axis ratio $b/a = 0.94 \pm 0.07$, at a projected distance of $\sim 0''.6$ or $3.4 \pm 0.2 \text{ kpc}$ from the quasar. All of these results assume that the source is at the same redshift as the quasar, but Marshall et al. cautioned that the southern source might be too bright to be a galaxy at the same redshift as the

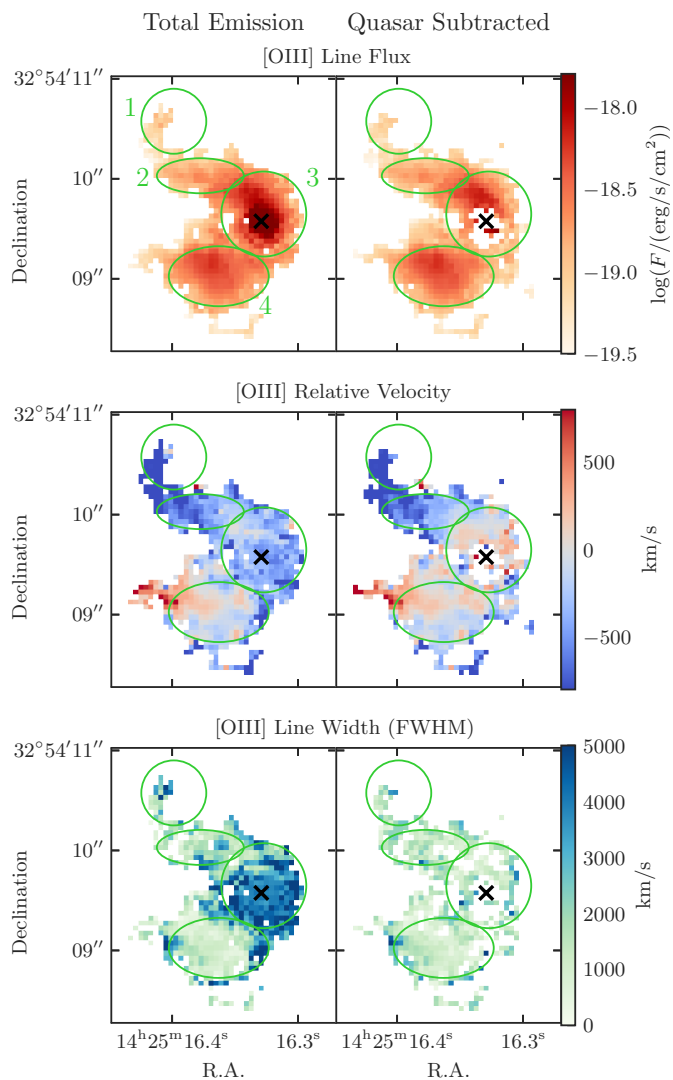


Fig. 5. Maps of the [O III] $\lambda 5007$ emission line regions surrounding NDWFS J1425+3254. From top to bottom, the panels show the line flux, velocity, and line width. The left column shows the data cubes containing both the quasar and extended emission, while the right column shows the cubes after the quasar has been subtracted. The location of the quasar is marked as a black cross, and the emission line region apertures from Figure 1 are included for reference. The line velocities and widths were measured from Gaussian fits to the lines in each spaxel; the velocity was measured as the line centre relative to the quasar host redshift of $z = 5.901$, and the width is the FWHM corrected for the instrumental resolution of 1966 km s^{-1} .

quasar. Our new IFU data give a clear detection of [O III] $\lambda 5007$ at the same south-east location (“Region 4”), confirming that this is indeed a very bright companion galaxy of the quasar.

Overall, we spectroscopically confirm the presence of two companion galaxies around the quasar, and discover a bridge of gas connecting the northern companion to the quasar host. We now study the physical properties of these regions.

4.2. Gas properties of the emission-line regions

Figure 6 shows the flux maps for [O III] $\lambda 5007$, H β , H α , and [N II] $\lambda 6584$, after quasar subtraction. The [O III] $\lambda 5007$ emission has the largest S/N and therefore is the clearest tracer of the

emission structures. H α generally follows the [O III] $\lambda 5007$ spatial distribution, while the S/N for H β and [N II] $\lambda \lambda 6548, 6584$ are too low for these to be detected across the whole system on a spaxel-by-spaxel basis. We integrated the spectral cube within each of the Figure 1 region apertures to obtain a spectrum for each region. Figure 7 shows these spectra across the wavelengths covering the relevant lines. We fit each spectrum with a single Gaussian for each emission line, tying all lines to have the same central velocity and physical velocity width, and fixing the [O III] $\lambda \lambda 4959, 5007$ and [N II] $\lambda \lambda 6548, 6584$ doublet ratios as in Section 2.3.4. Table 2 gives the fluxes and ratios, the Gaussian central velocity, v_r , and the Gaussian velocity width v_σ , corrected for instrumental resolution.

Region 1, the faintest emission-line region, has significant detections of [O III] $\lambda 5007$, H α and [N II] $\lambda \lambda 6548, 6584$, although with low S/N , with no detection of H β . All other regions also have significant H β and [O III] $\lambda 4959$ detections.

4.2.1. Photoionisation mechanisms

From these emission lines, we can estimate the dominant cause of gas photoionisation using the classical BPT diagnostic diagram (Baldwin et al. 1981), presented in Figure 8. All four regions lie within the area of the diagram typically populated by low- z AGN. This is expected for the quasar host, but the line ratios suggest that the two companions and gas bridge are also likely photoionised by AGN. We see no evidence for a point-source emitter suggestive of a type 1 AGN in either companion galaxy, and therefore photoionisation is likely from the quasar NDWFS J1425+3254 itself. However, an obscured AGN in one or both companions remains a possibility. Higher-resolution spectra would give a more accurate measurement of the [N II] $\lambda 6584/H\alpha$ flux ratios, which could be biased by the blending of the lines at our spectral resolution. Measurements of additional emission lines such as [S II] $\lambda \lambda 6716, 6731$ and [O I] $\lambda 6300$ would allow for other diagnostic methods to be used (e.g., Veilleux & Osterbrock 1987)—these were not detected in our spectra.

4.2.2. Nebular dust attenuation

The nebular dust attenuation can be estimated from the observed flux ratio of narrow H α to H β , as the theoretical non-extincted ratio is $F_{H\alpha}/F_{H\beta} \approx 2.86$, assuming a temperature of $T = 10^4$ K and an electron density $n_e = 10^2 \text{ cm}^{-3}$ for Case B recombination (Hummer & Storey 1987). Following Domínguez et al. (2013), the nebular colour excess can therefore be calculated as $E(B - V) = 1.97 \log_{10}[(F_{H\alpha}/F_{H\beta})/2.86]$ mag, and the attenuation in magnitudes at the wavelength λ can be calculated as $A_\lambda = k(\lambda)E(B - V)$, where $k(\lambda)$ is the reddening curve. Assuming the Calzetti et al. (2000) reddening law with $R_V = 4.05$, the attenuation of H α is $A_{H\alpha} = (3.33 \pm 0.80) \times E(B - V)$.

In regions where photoionisation has a significant contribution from AGN, additional collisional excitation of H α results in a larger H $\alpha/H\beta$ ratio than 2.86 (Ferland & Netzer 1983; Halpern & Steiner 1983; Osterbrock 1989). This means that for all of our emission lines, which all lie within the AGN region of the BPT diagram, we expect that the intrinsic flux ratio $F_{H\alpha}/F_{H\beta} \geq 2.86$. Therefore, our calculated attenuation values will be upper limits.

Table 3 lists the derived attenuation values based on the measured H $\alpha/H\beta$ ratios (Table 2). In the north-east companion (Region 1), H β is undetected, and so the attenuation is unconstrained but consistent with zero. The gas bridge (Region 2) has a low $F_{H\alpha}/F_{H\beta}$ ratio consistent with zero attenuation. The host galaxy

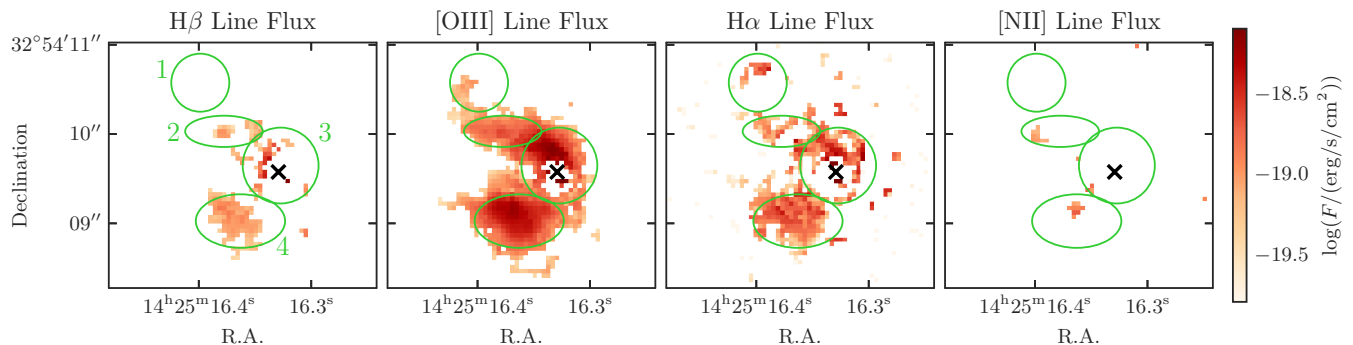


Fig. 6. Maps of the emission-line regions surrounding NDWFS J1425+3254 after the quasar emission has been subtracted. From left to right, the panels show the surface brightnesses of $H\beta$, $[O\text{ III}]\lambda 5007$, $H\alpha$, and $[N\text{ II}]\lambda 6584$. The $[O\text{ III}]\lambda 5007$ and $[N\text{ II}]\lambda 6584$ surface brightnesses are from fits with the doublet flux ratios constrained (Table 2 note). The location of the quasar is marked as a black cross, and the emission line region apertures from Figure 1 are marked in green.

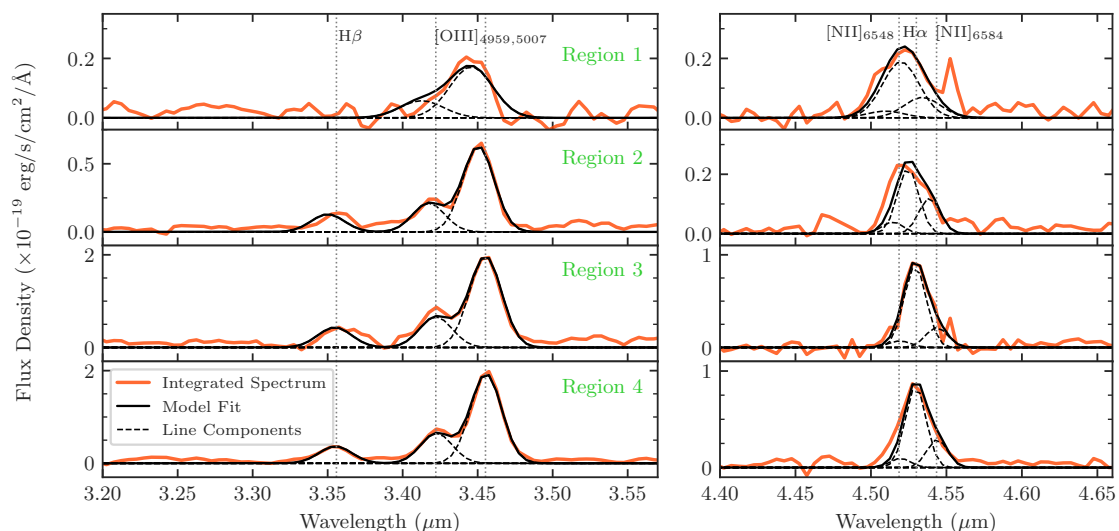


Fig. 7. The integrated spectrum for the emission line regions surrounding NDWFS J1425+3254 (orange), along with the best fit model (black solid). The individual Gaussian model components of $H\beta$, $[O\text{ III}]\lambda\lambda 4959, 5007$, $H\alpha$, and $[N\text{ II}]\lambda\lambda 6548, 6584$ are shown as dashed lines. The doublets are constrained to have a flux ratio of 2.98 for $[O\text{ III}]\lambda 5007/[O\text{ III}]\lambda 4959$ and 3.05 for $[N\text{ II}]\lambda 6584/[N\text{ II}]\lambda 6548$. The dotted vertical lines mark the emission line locations at the quasar host redshift, $z = 5.901$.

(Region 3) and south-east companion (Region 4) appear to have non-zero attenuation, with $A_{H\alpha} = 1.9^{+0.8}_{-1.1}$ mag for the host and $A_{H\alpha} = 0.9 \pm 0.2$ mag for the companion.

4.2.3. Star-formation rates

If the $H\alpha$ emission is excited by ionising photons from hot stars, the $H\alpha$ flux measures the star-formation rate (SFR). With no dust attenuation, a solar abundance, and a Kroupa (2001) IMF, the SFR can be estimated as:

$$\text{SFR} = 5.37 \times 10^{-42} \frac{L_{H\alpha}}{(\text{erg s}^{-1})} M_{\odot} \text{ yr}^{-1} \quad (3)$$

(Kennicutt & Evans 2012). Table 3 lists the implied SFRs for each region, both as observed and after correction for dust attenuation. These are all upper limits because, according to the BPT diagram, all regions have photoionisation from AGN and not purely star formation.

For the host galaxy (Region 3) the resulting dust-corrected SFR distribution has median of $258 M_{\odot} \text{ yr}^{-1}$, with a 3σ upper

limit (from the 99.87th percentile) of $<1600 M_{\odot} \text{ yr}^{-1}$. As well as the AGN contribution to photoionisation, this SFR measurement is further complicated by residual quasar contamination from the subtraction process. Also, the host's dust attenuation is uncertain, leading to a poorly-constrained dust-corrected SFR. This host SFR is consistent with the SFR estimate from the FIR luminosity (Wang et al. 2010) of $1160 M_{\odot} \text{ yr}^{-1}$, but without dust correction the SFR estimate is much smaller. On its face, this comparison suggests that most of the star formation in the quasar host is heavily obscured. However, many effects make this comparison difficult: the FIR and $H\alpha$ trace star formation on different timescales, with the FIR sensitive to star formation to $\gtrsim 100$ Myr ago, while the $H\alpha$ captures stars formed over only the past ~ 10 Myr (Kennicutt & Evans 2012); the FIR observations have poor spatial resolution and include the flux from all four regions; and there is potential for significant contamination by the quasar for both measurements (e.g., Tsukui et al. 2023).

NDWFS J1425+3254 was originally targeted in the HST program due to its bright FIR luminosity and relatively faint UV luminosity (relative to comparable high- z quasars), with

Table 2. Fluxes and velocities for the H β , [O III] λ 5007, H α , and [N II] λ 6584 galaxy line components for each emission line region as defined in Figure 1, measured from the integrated spectra shown in Figure 7.

Reg.	$F_{\text{H}\beta}$	$F_{[\text{OIII}]}$ (10^{-18} erg s $^{-1}$ cm $^{-2}$)	$F_{\text{H}\alpha}$ [S/N]	$F_{[\text{NII}]}$	$F_{\text{H}\alpha}/F_{\text{H}\beta}$	$F_{[\text{OIII}]} / F_{\text{H}\beta}$	$F_{[\text{NII}]} / F_{\text{H}\alpha}$	v_r (km s $^{-1}$)	v_σ (km s $^{-1}$)
1	<1.8 (3 σ)	6.2 \pm 0.6 [11]	7.5 \pm 0.9 [9]	3.3 \pm 1.2 [3]	>2.7 (3 σ)	>2.5 (3 σ)	0.4 \pm 0.2	-820 \pm 217	951 $^{+317}_{-417}$
2	2.1 \pm 0.2 [9]	16.6 \pm 0.4 [40]	5.1 \pm 0.4 [13]	4.2 \pm 0.6 [7]	2.5 \pm 0.3	8.1 \pm 0.9	0.83 \pm 0.14	-408 \pm 217	425 $^{+434}_{-425}$
3	3.9 \pm 1.2 [3]	53.3 \pm 1.7 [31]	21.3 \pm 2.1 [10]	7.6 \pm 2.6 [3]	5.5 \pm 1.8	13.8 \pm 4.4	0.36 \pm 0.13	0 \pm 217	466 $^{+419}_{-466}$
4	4.8 \pm 0.3 [16]	50.6 \pm 0.6 [88]	18.9 \pm 0.5 [36]	10.0 \pm 0.8 [12]	3.9 \pm 0.3	10.5 \pm 0.6	0.53 \pm 0.05	36 \pm 217	403 $^{+443}_{-403}$

Notes. The [O III] λ 4959, 5007 doublet is constrained to have a flux ratio of [O III] λ 5007/[O III] λ 4959 = 2.98, and [N II] λ 6548, 6584 is constrained to have a flux ratio of [N II] λ 6584/[N II] λ 6548 = 3.05. The tabulated fluxes are for the brighter line of each pair. The values in braces give the integrated S/N of each line. Upper limits for undetected lines are 3 σ , taken from the rescaled ERR array accounting for the quasar subtraction uncertainty (Section 2.3.3). The central velocities are defined relative to the host central velocity at $z = 5.901$. Uncertainties on the velocity and velocity dispersion assume a measurement uncertainty of 0.5 wavelength elements, $\pm 25 \text{ \AA}$ which corresponds to 217 km s $^{-1}$ at [O III] λ 5007. The velocity dispersions are the physical velocity widths, corrected for instrumental resolution (where FWHM $v_{\text{inst}} = 1966 \pm 178$ km s $^{-1}$ for [O III] λ 5007 from Appendix B; these uncertainties are incorporated into the velocity dispersion uncertainty).

Table 3. Physical properties calculated for the emission line regions: nebular dust attenuation $A_{\text{H}\alpha}$, SFR, dust-corrected SFR, mass-to-light ratio M_*/L in the HST/WFC3 F160W filter, stellar age t , metal abundance $[M/H]$, stellar dust attenuation A_V , and stellar mass M_* .

Region	$A_{\text{H}\alpha}$ (mag)	SFR (M_\odot yr $^{-1}$)	SFR $_{\text{dust-corr.}}$ (M_\odot yr $^{-1}$)	M_*/L ($10^{-4} M_\odot/L_\odot$)	t (Myr)	$[M/H]$	A_V (mag)	M_* ($10^{10} M_\odot$)
1	≥ 0	16.1 \pm 1.9	–	14 $^{+3}_{-1}$	65 $^{+9}_{-4}$	> -0.1	0.41 $^{+0.04}_{-0.05}$	36 $^{+6}_{-3}$
2 (2*)	<0.5 (3 σ)	11.0 \pm 0.8	–	1.6 $^{+2.0}_{-0.7}$	8 $^{+10}_{-4}$	–	–	–
3	1.9 $^{+0.8}_{-1.1}$	46.1 \pm 4.5	258 $^{+288}_{-167}$	–	–	–	–	–
4 (4*)	0.9 \pm 0.2	40.9 \pm 1.2	93 $^{+17}_{-16}$	0.7 $^{+0.2}_{-0.1}$	6.7 $^{+1.8}_{-1.8}$	< -0.8	1.2 $^{+0.1}_{-0.1}$	1.9 $^{+0.4}_{-0.4}$

Notes. The properties $A_{\text{H}\alpha}$, SFR, and SFR $_{\text{dust-corr.}}$ are based on the H α and H β narrow-line fluxes listed in Table 2, following the equations in Sections 4.2.2 and 4.2.3. The true SFRs are likely to be smaller than the calculated values because the quasar contributes to the photoionisation. The nebular dust quantities are also upper limits as $F_{\text{H}\alpha}/F_{\text{H}\beta}$ can be larger than 2.86 for AGN photoionisation. The stellar population properties t , $[M/H]$, and A_V were calculated from the pPXF SPS modelling (Section 4.3). These models used the smaller Regions 2* and 4* to avoid contamination by the quasar. These SPS quantities are light-weighted values. The stellar mass M_* was calculated from the SPS mass-to-light-ratio and the HST/WFC3 F160W H -band magnitude of the two companion galaxies. Region 2 was undetected in the H -band images, prohibiting a stellar mass estimate. Region 3 is dominated by the quasar emission, and no SPS fitting is possible.

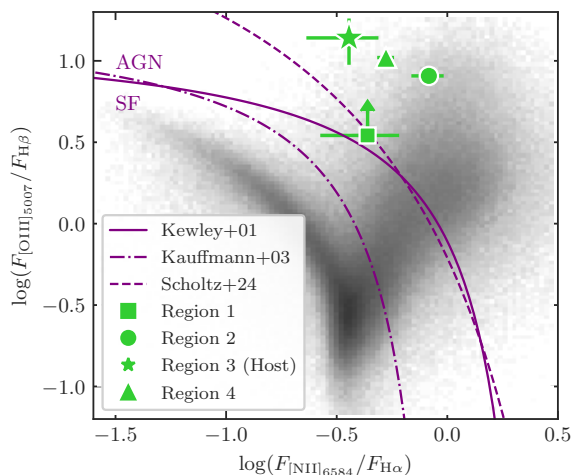


Fig. 8. The BPT diagnostic diagram (Baldwin et al. 1981) showing the narrow emission line ratios $F_{[\text{NII}]\lambda 6584}/F_{\text{H}\alpha}$ and $F_{[\text{OIII}]\lambda 5007}/F_{\text{H}\beta}$. The Kewley et al. (2001), Kauffmann et al. (2003), and Scholtz et al. (2024) demarcation curves distinguish the regions where photoionisation is dominated by galaxies (lower left) and AGN (upper right), as determined for low- z objects. The underlying grey histogram shows local sources from the SDSS (Abazajian et al. 2009).

$F_{250\text{GHz}}/F_{1\mu\text{m}} \simeq 100$ (Marshall et al. 2020). A high FIR luminosity implies a large SFR and thus an intrinsically bright host, which combined with the lower UV luminosity may result

in a less extreme quasar-to-host contrast ratio and thus improved detectability of the host via quasar subtraction. This selection is consistent with our finding of significant ongoing, but obscured, star formation. With such a FIR excess, it is unsurprising that this luminous infrared galaxy (LIRG)-like quasar host is undergoing galaxy mergers, as LIRGs are commonly found to have merger-induced star formation and AGN activity (e.g., Veilleux et al. 2002; Younger et al. 2009).

The south-east companion (Region 4) has significant H α emission, and unless this is entirely powered by the AGN, this galaxy must have moderate ongoing star formation. The north-east neighbour (Region 1) has weaker observed H α flux but could have high attenuation. If this north-east companion is undergoing as much star formation as in the host and the southern neighbour, it must be predominantly obscured. The bridge (Region 2) has the weakest measured H α flux, which could be caused by star formation at a rate of up to $11 \pm 0.8 M_\odot \text{ yr}^{-1}$, or entirely by the AGN photoionisation (see also Section 6.4).

4.2.4. Kinematics

As the spectral resolution of these observations is only $R \sim 100$, all measured velocities and velocity dispersions have significant uncertainty, as well as there being significant uncertainty in the measured LSF. Nevertheless, the general, relative velocity trends shown in the [O III] λ 5007 maps (Figure 5) should be accurate. The northern companion is blueshifted relative to the quasar host, there is a velocity gradient across the connecting bridge extending

to the velocity of the quasar host, and the southern companion has a redshifted velocity relative to the quasar. There is significant spatially-unresolved broad [O III] $\lambda\lambda 4959, 5007$ emission from the quasar, likely from a strong outflow, while the remainder of the emission structures exhibit much lower velocity dispersions. However, the specific velocity quantities are uncertain, as reflected by the quoted uncertainties. Indeed the velocity dispersions for Regions 2, 3, and 4 from Table 2 are all consistent with zero within 1σ . Even the apparent velocity dispersion for Region 1 (confidence interval 534–1268 km s^{-1}) is based on low S/N , and $H\beta$ is undetected. It is likely that this large velocity is biased rather than truly $>500 \text{ km s}^{-1}$. Higher spectral resolution data of this system, particularly with the NIRSpect IFU $R \sim 2700$ grating, would allow a more quantitative study of the velocities within this system (as in e.g., Arribas et al. 2024; Fujimoto et al. 2024; Jones et al. 2024; Marconcini et al. 2024; Parlanti et al. 2024a,b; Rodríguez Del Pino et al. 2024; Übler et al. 2024a). Given the uncertainties, we generally avoid placing significance on the measured velocities in this work and instead focus on the line fluxes and associated physical properties.

4.3. Stellar properties of the emission-line regions

Figure 9 shows the integrated spectra for Regions 1, 2* and 4*, the smaller subsets of Regions 2 and 4 (see Figure A.1). These data, used for fitting the continuum emission with pPXF, have two main differences from the spectra in Figure 7. Firstly, these spectra were taken from the original cube containing the continuum emission. Secondly, Regions 2* and 4* are smaller than Regions 2 and 4, defined to exclude most of the quasar emission and thus give an un-contaminated, accurate spectral shape for the companion sources. This allows SPS modelling, although the smaller area does not contain all of the flux of each source. Region 3 cannot be studied in this way because the quasar contaminates the entire source.

We use pPXF to fit stellar population models to these spectra as described in Section 2.3.5, with Table 3 listing the output ages and metallicities of the stellar populations. All of the companion regions show clear continuum emission across the rest-frame UV, with Region 1 also showing significant emission at rest-frame wavelengths $\gtrsim 3800 \text{ \AA}$. The northern companion Region 1 shows a clear Balmer break from the older stellar population. The metallicity is poorly constrained but relatively high. For the connecting bridge, Region 2*, the low S/N and spectral resolution mean pPXF cannot constrain the metal abundance or stellar dust attenuation, but the blue UV slope and lack of Balmer break suggest a young stellar population. For the southern companion, Region 4*, pPXF measures a similarly young stellar age, modest but non-zero stellar dust attenuation, and low metal abundance.

From these stellar population models and the resulting mass-to-light ratio estimates, we estimate the stellar masses for the emission regions. We cannot determine the total flux of these regions from the IFU spectra, due to contamination by the quasar emission. We therefore used HST/WFC3 photometry with the quasar flux subtracted (Marshall et al. 2020) to give accurate H -band fluxes of the northern and southern companions: $m_H = 24.2$ mag for Region 1, and $m_H = 24.3$ mag for Region 4. Table 3 gives the resulting stellar masses and the estimated mass-to-light ratios from the SPS fitting from which they were calculated. The connecting gas bridge was undetected in the WFC3 images, and so no stellar mass estimate is possible in this manner.

The northern companion has an older, massive stellar population that is relatively metal-rich, while the southern companion is younger, less massive, and metal-poor. The stellar mass of the northern companion, $(3.6^{+0.6}_{-0.3}) \times 10^{11} M_\odot$, is equivalent to the most massive galaxies observed at these redshifts (Xiao et al. 2024). Given its SFR of $16.1 \pm 1.9 M_\odot \text{ yr}^{-1}$, the northern companion lies significantly below the star-forming main sequence (offset by ~ -1.3 dex, Popesso et al. 2023). In contrast, the less massive but more highly star-forming southern companion lies on the star-forming main sequence (Popesso et al. 2023). The southern companion has more dust attenuation than the northern one, despite the northern companion’s larger mass and older stellar population.

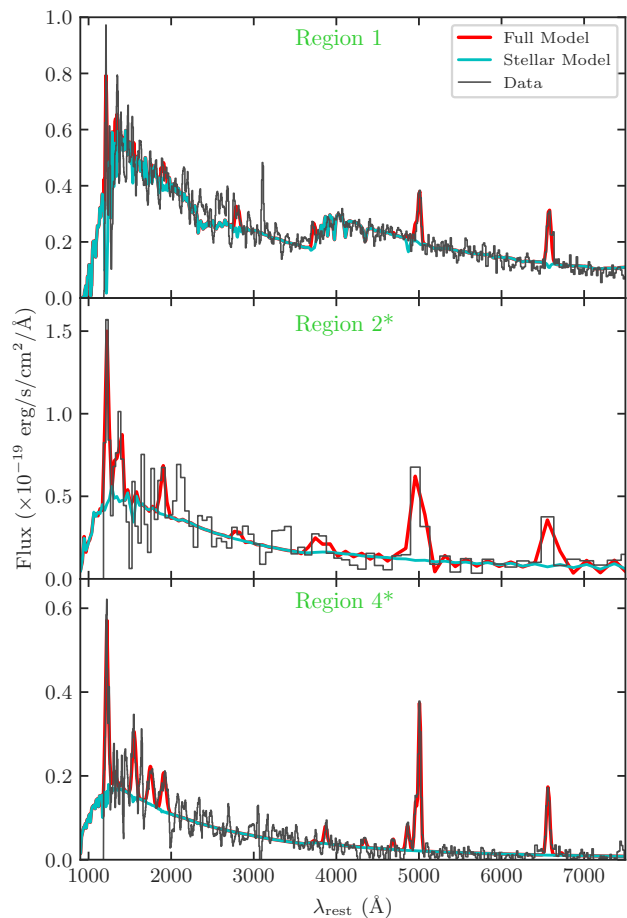


Fig. 9. Spectra for Regions 1, 2*, and 4* (black), integrated over the apertures shown in Figure A.1. The red curve shows the full gas and stellar model as fit by pPXF for each region, with the stellar component shown in blue. These spectra are taken from the original data cube, which includes the continuum emission and the quasar flux. The apertures for Regions 2* and 4* are reduced in size from Regions 2 and 4, to exclude the portion that contains flux from the quasar and thus ensure an accurate measurement of the stellar population. The spectrum for Region 2* has been rebinned on to a $10\times$ coarser wavelength grid to obtain a higher S/N , as on the original grid the continuum has $S/N \lesssim 5$.

5. Foreground Lensing Source

The IFU data cube shows an additional source $0''.81$ north-northwest of the quasar, discovered via its two bright emission lines at $1.07 \mu\text{m}$ and $1.40 \mu\text{m}$. Figure 10 shows the location of

this source and its extracted spectrum. There is clear continuum emission between ~ 1 and $3 \mu\text{m}$, with the emission also detectable in the HST/WFC3 F125W and F160W images with $m_J = 28.8$ mag and $m_H = 26.9$ mag. There is an additional emission line present in the spectrum at $0.85 \mu\text{m}$, but this emission is purely contamination from the nearby quasar’s Lyman- α . Given the spatial proximity to the quasar, this source could potentially be a foreground galaxy that may act as a gravitational lens for the quasar, or alternatively this could be a background galaxy that could be lensed by the quasar.

The most likely redshift solution for the two emission lines is $z = 1.135 \pm 0.010$, which would identify the lines as [O III] $\lambda 5007$ and H α , respectively. The asymmetry of the $1.07 \mu\text{m}$ line is consistent with being a blend between the doublet [O III] $\lambda\lambda 4959, 5007$ and potentially H β , providing additional support for this redshift solution. Unfortunately, these lines fall in the spectral region with the lowest resolution, $R \approx 35$ or $v_{\text{inst}} \approx 8400 \pm 800 \text{ km s}^{-1}$. Combined with the issue that the $1.07 \mu\text{m}$ line would be a blend of lines, and that H α could be blended with [N II] $\lambda\lambda 6548, 6584$, the current data cannot measure the physical line widths of this system. Higher-resolution spectra would give a velocity measurement of this galaxy, as well as verifying the line identifications.

If the presumed foreground galaxy has significant mass and is at $z = 1.135$, it will gravitationally lens the background quasar. If the lensing galaxy is a singular isothermal sphere with stellar velocity dispersion σ is between 50 and 145 km s^{-1} , the quasar would always lie outside the caustic in the source plane, and therefore not be multiply imaged. Such configurations have magnifications $1 < \mu < 2$, or < 0.75 mag. If the galaxy’s stellar velocity dispersion $\sigma \gtrsim 150 \text{ km s}^{-1}$, the lens would produce a secondary image of the quasar. However, we do not see a secondary image in the deep observations available, and thus such high velocity dispersion is ruled out. Because the lens magnification of the quasar and the companions should be small, we have not applied any lensing correction. Precise line-width measurements for the lens could determine the actual amount of lensing.

The spectrum admits an alternative redshift solution $z = 7.018 \pm 0.010$ for the north-west galaxy. In this case, the $1.07 \mu\text{m}$ line would come from [C II] $\lambda 1334$ and the $1.40 \mu\text{m}$ line from N III] $\lambda 1747$. This scenario is unlikely because we would also expect to see the typically much brighter galaxy lines such as Mg II $\lambda 2799$, [O II] $\lambda 3727$, [O III] $\lambda\lambda 4959, 5007$, and the Hydrogen Balmer series, yet no additional emission lines are detected; the presence of only two emission lines and the blue continuum are more consistent with the $z = 1.135$ solution. Furthermore, if this source were at $z = 7.018$, we would expect to see no continuum flux at wavelengths below the Lyman- α break at $0.975 \mu\text{m}$. The noise in the IFU spectrum significantly increases at the bluest wavelengths, making this measurement difficult. However, summing the flux across the wavelength region $0.7\text{--}0.975 \mu\text{m}$, excluding wavelengths $0.81\text{--}0.88 \mu\text{m}$ which contain flux from the quasar’s Lyman- α line, gives a positive detection $f_{<0.975\mu\text{m}} = (5.3 \pm 0.6) \times 10^{-17} \text{ erg s}^{-1} \text{ cm}^{-2}$. The presence of statistically significant flux blue-ward of Lyman- α makes it unlikely that the source is at $z = 7.018$, favouring the $z = 1.135$ solution.

If this source is a background galaxy at $z = 7.018$, it would likely be gravitationally lensed by the foreground quasar. We estimate the quasar host’s stellar velocity dispersion from our black hole mass measurement using the Greene et al. (2020) $M_{\text{BH}}\text{--}\sigma_*$ scaling relation. Assuming that the quasar host system is a singular isothermal sphere with $\sigma_* = 310_{-100}^{+140} \text{ km s}^{-1}$, we calculate that the background galaxy would not be multiply imaged, with

magnifications $1 < \mu < 2$, or < 0.75 mag. However, we reiterate that the $z = 1.135$ solution is more likely, in which case it is this galaxy that is weakly lensing the background quasar. A higher-resolution spectrum is needed to definitively confirm the redshift of this galaxy.

6. Discussion

6.1. Host stellar mass

In this work we are unable to estimate the stellar mass of the host galaxy, Region 3. As discussed in Section 2.3.5, we cannot perform SPS modelling for the host, as this requires a spectrum of the galaxy continuum emission across a broad wavelength range, which is not possible to produce with our quasar subtraction technique. Developing a quasar-subtraction strategy that allows for stellar mass measurements will require significant additional work, and so this will be the focus of a future study.

There are two existing mass estimates for the quasar host in the literature. From the CO emission, Wang et al. (2010) estimated a dynamical mass $M_{\text{dyn}} \geq 1.56 \times 10^{11} M_{\odot}$. However, the resolution of these PdBI observations was FWHM $\sim 5''$, making this estimate very uncertain. An upper limit on the host mass came from non-detections of the host in the PSF-subtracted J - and H -band HST imaging (Marshall et al. 2020). With significant assumptions, Marshall et al. placed an upper limit $M_* < 1.5 \times 10^{11} M_{\odot}$. These measurements likely imply that the quasar host galaxy is less massive than the northern companion, and probably as massive as the southern companion (Table 3). However, both observations and resulting mass measurements have significant limitations, and these mass limits are difficult to interpret in the context of the companion galaxies.

The lack of accurate host stellar mass measurement results in two significant drawbacks to the current interpretation of ND-WFS J1425+3254. Firstly, we are limited in understanding the merger physics for this system. Without a host galaxy mass measurement, it is unclear whether the mergers with the northern and southern companion are ‘major’ mergers, and whether the host is the most massive galaxy in this merging system. Statistically we may expect that the quasar would reside in the most massive galaxy in the system (Keel 1996), however the current stellar mass limit suggests that this is not the case. Secondly, we cannot study the black hole–stellar mass relation for this quasar. Observations with JWST (Yue et al. 2024; Kokorev et al. 2023; Juodžbalis et al. 2024; Maiolino et al. 2023; Marshall et al. 2024) have been finding high- z black holes that lie significantly above the local relations, and it would be interesting to see whether the black hole in this extreme merging system is similarly overmassive. The local black hole–stellar mass relation from Greene et al. (2020) says that a black hole with mass $M_{\text{BH}} = (1.4_{-1.0}^{+3.1}) \times 10^9 M_{\odot}$ will have a host galaxy with stellar mass $M_{*,\text{host}} = (3.6_{-0.9}^{+10.4}) \times 10^{11} M_{\odot}$, similar in mass to the northern companion. However, an extreme black hole–stellar mass ratio similar to other high- z quasars of $\sim 10\text{--}50\%$ (Yue et al. 2024; Marshall et al. 2024) would result in $M_{*,\text{host}} \approx 0.3\text{--}1.4 \times 10^{10} M_{\odot}$, less massive than even the southern companion galaxy. Obtaining stellar mass estimates for the host would lead to much clearer insights on both topics. A better mass estimate will require better subtraction of the quasar flux or some indirect method.

6.2. Merger dynamics

The lack of an accurate stellar mass for the quasar host means we cannot determine which galaxy is the most massive ‘central’

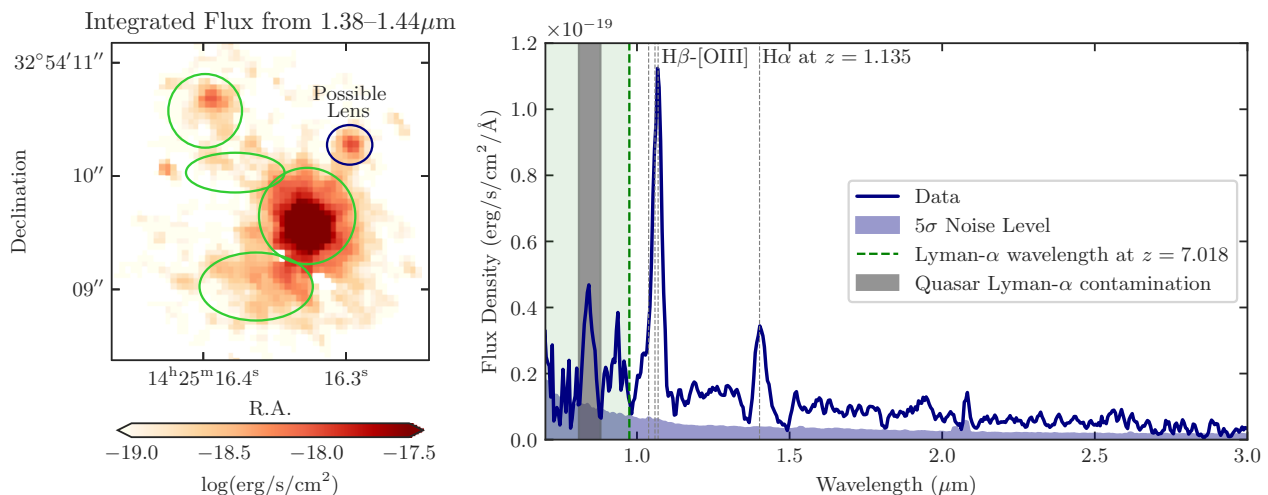


Fig. 10. *Left:* The flux from the full data cube integrated across 1.38–1.44 μm . The emission-line region apertures from Figure 1 are included for reference (green). A fifth aperture (black) marks the additional flux source 0''81 to the north-northwest of the quasar. *Right:* The spectrum integrated over the black aperture in the left panel (blue). Three clear emission lines are seen at 0.85 μm , 1.07 μm and 1.40 μm . The 0.85 μm line is contaminating Lyman-alpha flux from the nearby quasar (grey shaded wavelengths). There are two potential redshift solutions for the 1.07 μm and 1.40 μm emission lines: $z = 1.135$ for the [O III] $\lambda 5007$ and H α emission lines (dashed grey lines) or $z = 7.018$ from [C III] $\lambda 1134$ and N III] $\lambda 1747$. The green dashed line marks the Lyman- α redshift at $z = 7.018$, below this in the green shaded region we would expect no flux for a high- z galaxy. In fact, this region shows significant continuum flux, suggesting that this source is at $z = 1.135$.

galaxy in the NDWFS J1425+3254 system. The Marshall et al. (2020) upper limit for the host ($M_* < 1.5 \times 10^{11} M_\odot$) makes it most likely that the northern companion galaxy with $M_* = (3.6^{+0.6}_{-0.3}) \times 10^{11} M_\odot$ is the central galaxy. This section describes the merger dynamics assuming that this is the case. However, the quoted dynamics are all relative, and the same analysis applies.

The velocity offset of -820 ± 217 km/s between the quasar host and the northern companion (Table 2) can have a contribution from two components: Hubble flow with the companion at a different cosmological distance than the host (i.e. a different cosmological redshift), and a physical (“peculiar”) velocity of the companion relative to the quasar. If there is no peculiar velocity, the northern companion would be 1.2 pMpc nearer than the quasar in the adopted cosmology. However, the clear presence of a connecting gas bridge between the quasar and companion rules out this scenario. The velocity of the gas bridge varies smoothly between the quasar and companion, connecting the two, which would require the gas bridge to be over 1 Mpc long—clearly unphysical. Indeed, requiring a physical separation $d_z < 100$ kpc, a generous maximum for a connecting-bridge scenario, requires a cosmological redshift difference no more than 1/12 of the actual redshift difference. Therefore, nearly all of the ~ 820 km/s velocity offset between the companion and quasar must be a physical velocity, with the two at a similar cosmological distance.

The Cool et al. (2006) discovery spectrum has a significant decrease in flux from ~ 8360 – 8380 \AA , between the Lyman- α and N V $\lambda 1240$ line. Mechtley (2014) determined that this is most likely foreground H I $\lambda 1216$ \AA absorption from a companion galaxy, although alternate explanations including blueshifted N V are possible. Such an absorption wavelength corresponds to a redshift of $z = 5.875$ – 5.891 or between -1100 and -400 km s^{-1} relative to the quasar host at $z = 5.901$, consistent with the measured velocity of the northern companion. Therefore the absorption feature is likely from the northern companion galaxy which lies in the foreground, with the quasar moving away from both us and the companion at ~ 820 km s^{-1} . This suggests that the quasar was once in front of the companion galaxy, fell in towards the companion, and has now made its first pass and has begun to travel away.

The dynamical timescale at $z = 5.9$ is ~ 150 Myr, while the total age of the Universe at this time is 965 Myr. The expected merger timescale depends strongly on mass ratio and orbital eccentricity but will typically be of the order of the dynamical time (Jiang et al. 2008; Boylan-Kolchin et al. 2008), as will the dynamical friction timescale (Binney & Tremaine 1987). The stellar ages (Table 3) for both companions are significantly less than the dynamical time. This implies that the star formation in the galaxies most likely began while the galaxy interaction was in progress. Lower- z studies have found that SFRs are significantly enhanced at pair separation distances of $\lesssim 25$ kpc (Shah et al. 2022) or potentially 100s of kpc (Patton et al. 2020). With a current physical separation of $d_z < 100$ kpc, and with the quasar likely travelling only ~ 55 kpc in the ~ 65 Myr since the northern companion’s star formation began (assuming constant speed of 820 km s^{-1}), the pair separation at the onset of the star formation was within this region of potential interaction-induced star formation. Therefore, star formation in the companions having been triggered by the merger is a plausible scenario. Indeed, it is also possible that the interaction has induced the quasar activity (Byrne-Mamahit et al. 2024).

The presence of the gas bridge provides further evidence that the quasar has already been through its first pass of the northern companion. As the quasar approached the companion, the interaction triggered an episode of star formation in the companion. After the close fly-by, the gas was tidally torn away from the galaxy outskirts, creating a tidal bridge (Toomre & Toomre 1972; Wright 1972; Oh et al. 2008). The bridge is clear evidence for an ongoing interaction between the northern companion and the quasar host galaxy.

The relative dynamics of the southern companion are more difficult to constrain, given the lack of a connecting gas bridge. However, this companion has a negligible velocity offset from the quasar host of 36 ± 217 km/s, strongly suggesting that it is associated with the quasar.

These various interacting galaxies must live the same dark-matter halo. One way to estimate the halo mass is from the stellar mass of the central galaxy. That must be at least the mass of the northern companion, but potentially the mass of

a more massive quasar host. Applying the stellar–host mass relation (Girelli et al. 2020; Shuntov et al. 2022) to the northern companion stellar mass gives a halo–mass estimate $M_h \simeq 10^{12.5} - 10^{13} M_\odot$. This implies a virial velocity of 500–650 km/s, and so the low-velocity southern neighbour would be strongly bound to the quasar. To bind the northern neighbour and quasar host, the virial velocity must be $\gtrsim 820 \pm 217$ km/s, consistent with a massive halo with $M_h \gtrsim 10^{13} M_\odot$. Such a halo has a virial radius $R_{\text{vir}} = 100(M_h/10^{13} M_\odot)^{1/3}$ kpc $= 17(M_h/10^{13} M_\odot)^{1/3}$ arcsec. That means that the inner core of the halo, which is all the IFU’s $3'' \times 3''$ FoV covers, contains three merging galaxies, one of which hosts a luminous quasar. This is a protocluster core that will evolve into an extremely massive $\gtrsim 10^{15} M_\odot$ cluster by $z = 0$ (e.g., Reed et al. 2003).

6.3. High- z quasars in galaxy mergers

NDWFS J1425+3254 joins a growing list of high- z quasars that are spectroscopically confirmed to be undergoing galaxy–galaxy mergers. PSO J308.0416–21.2339 at $z \simeq 6.2$ (Decarli et al. 2019) is accreting two massive $M_* \simeq 10^{10} M_\odot$ companion galaxies onto a quasar host with dynamical mass $M_{\text{dyn}} > 10^{11} M_\odot$. One of the companion galaxies is connected to the quasar via a bridge clearly detected in H α , H β , and [O III] $\lambda\lambda 4959, 5007$ (Loiacono et al. 2024; Decarli et al. 2024). DELS J0411–0907 at $z = 6.82$ has a companion galaxy with $M_{\text{dyn}} \simeq 2.5 \times 10^{10} M_\odot$ merging with an $M_{\text{dyn}} \simeq 8.6 \times 10^{10} M_\odot$ quasar host (Marshall et al. 2023). VDES J0020–3653 at $z = 6.86$ is merging with three companions, two of which have $M_{\text{dyn}} \simeq 1.5 \times 10^{11} M_\odot$ and $\simeq 8 \times 10^{10} M_\odot$ compared to host $M_{\text{dyn}} \simeq 1.7 \times 10^{11} M_\odot$ (Marshall et al. 2023). ULAS J112001.48+064124.3 at $z = 7.08$ is also merging with a bright companion galaxy, with $M_* \simeq 2.6 \times 10^9 M_\odot$ for the host and $M_* \simeq 5.0 \times 10^9 M_\odot$ for the companion galaxy (Marshall et al. 2024). BR 1202–0725 at $z \simeq 4.7$ is in a highly overdense system, with an abundance of nearby galaxies on kpc scales including a secondary AGN (Zamora et al. 2024). The quasar SDSS J113308.78+160355.7 at $z = 5.63$ has a prominent bridge between the host and a dust-obscured companion as revealed with ALMA (Zhu et al. 2024). In this case, the companion is undergoing intense star formation of $\sim 10^3 M_\odot \text{yr}^{-1}$. Neeleman et al. (2019) studied five quasars with ALMA that have companions at separations of 5–60 kpc; PSO J167.6415–13.4960 at $z = 6.51$ and SDSS J130608.25+035626.3 at $z = 6.03$ have connecting gas bridges between the companion and the quasar host. At $z = 6.05$ there is a pair of two merging quasars, separated by (projected) 12 kpc and with a connecting gas bridge (Matsuoka et al. 2024; Izumi et al. 2024). The extremely luminous galaxy WISE J224607.55–052634.9, which hosts a dust-obscured quasar at $z = 4.6$, is connected to multiple merging companion galaxies via dust streams (Díaz-Santos et al. 2018). The presence of gas bridges in all of these systems provides unambiguous evidence for significant ongoing interactions at high- z .

The great number of detections of merging high- z quasars suggests that the intense black hole growth may be induced or enhanced by the merger activity. Theoretically, mergers are expected to enhance both AGN and star formation (e.g., Doyon et al. 1994; Hernquist & Mihos 1995; Mihos & Hernquist 1996; Hopkins et al. 2006; Patton et al. 2020; Byrne-Mamahit et al. 2023, 2024). However, it is possible that the merger and the extreme black hole growth are unrelated and purely coincidental. Similar extreme environments, with gas bridges extending between star-forming and dusty galaxies, are seen at similar redshifts for non-quasar galaxies (e.g., Litke et al. 2019; Asada et al.

2023; Villanueva et al. 2024; Solimano et al. 2025, although these may show a different phase of the merger before or after induced quasar activity). A detailed investigation of the fraction of both quasars and similar galaxies undergoing mergers at these redshifts is needed for a clearer conclusion on the link between mergers and early black hole growth.

6.4. Quasar–companion cross-ionisation

As shown in Section 4.2.1, the two companion galaxies and the connecting bridge are likely photoionised by AGN photons. It has been observed in other systems that a central AGN may photoionise nearby companion galaxies (so called “cross-ionisation”; e.g., Moran et al. 1992; da Silva et al. 2011; Merluzzi et al. 2018; Keel et al. 2019; Moiseev et al. 2023; Protušová et al. 2024). The intrinsic [O III] $\lambda 5007$ surface brightness in the NDWFS J1425+3254 extended regions is a close match on ~ 10 kpc scales to that in the extended emission-line regions in Mrk 266, which has the highest surface brightness extended line emission seen in the local Universe (Keel et al. 2012a). These similarities raise the question of whether the quasar could be the source of ionisation for its companions.

For each of the companions, we calculated the ionising photon rate required to produce the observed H β luminosity

$$Q_{\text{comp}} = L_{\text{H}\beta} / (4.8 \times 10^{-13} \text{ erg}) \quad , \quad (4)$$

assuming that one H β photon (with energy 4.09×10^{-12} erg) is produced for every 8.54 recombinations (Hummer & Storey 1987). This gives required incident ionising-photon rates of $< 1.5 \times 10^{54} \text{ s}^{-1}$ (3σ), $1.7 \times 10^{54} \text{ s}^{-1}$, and $4.1 \times 10^{54} \text{ s}^{-1}$ for Regions 1, 2, and 4, respectively.

The incident ionising luminosity from the quasar onto a companion can be estimated as

$$L_{\text{q,incident}} = L_{\text{bol}} \gamma \frac{\Omega}{4\pi} \quad , \quad (5)$$

where γ is the ratio of ionising to bolometric luminosity, and Ω is the solid angle the companion subtends as seen from the quasar. For small angles, $\Omega = \pi(\arctan(r/d))^2$, assuming a spherical galaxy of radius r at distance d . For a typical quasar SED, $\gamma = 0.14$ (Keel et al. 2019). The extent of the [O III] $\lambda 5007$ flux (Figure 1) perpendicular to the direction of the quasar gives $r = 0''.21, 0''.25,$ and $0''.36$ for Regions 1, 2, and 4, respectively. We use the distance d from the centre of each galaxy to the centre of the quasar measured from Sérsic profile fits to the HST imaging (Marshall et al. 2020), $1''.4$ and $0''.6$ for Regions 1 and 4, respectively. The connecting bridge extends from the quasar to Region 1, with an average distance of $0''.7$. To convert ionising luminosity to an incident photon rate, we assume a mean ionising photon energy of 2 rydbergs or 4.36×10^{-11} erg, such that

$$Q_{\text{q,incident}} = L_{\text{q,incident}} / (4.36 \times 10^{-11} \text{ erg}). \quad (6)$$

For the three regions, this gives $Q_{\text{q,incident}} = 1.1 \times 10^{54} \text{ s}^{-1}, 5.3 \times 10^{54} \text{ s}^{-1},$ and $13.6 \times 10^{54} \text{ s}^{-1},$ respectively.

The incident photon rates from the quasar are at first glance sufficient to photoionise the two companions and the connecting bridge, with ratios of $Q_{\text{q,incident}}/Q_{\text{comp}} > 0.7, 3.1,$ and $3.4.$ However, these calculations assume the minimum possible distances based on the sky projection. De-projected distances will likely require larger ionisation luminosities. These calculations also do not include dust attenuation corrections. However, even if the

true $Q_{q,incident}/Q_{comp} < 1$, the companion galaxies could produce additional ionisation via star formation. Another possibility is that the quasar was previously more luminous and has faded, as seen for Hanny’s Voorwerp and other AGN-ionised clouds on timescales of $\sim 10^4$ – 10^5 yr. (Lintott et al. 2009; Schawinski et al. 2010; Keel et al. 2012b,a; Schirmer et al. 2013). While no definitive conclusion on the source of the companion-galaxy photoionisation is possible, the quasar luminosity appears sufficient to ionise the surrounding regions out to kpc scales.

7. Conclusions

In this work we present JWST NIRSpec IFU observations of the $z = 5.89$ quasar NDWFS J1425+3254, taken as part of the PEARLS GTO program. This prism spectra covers the wavelength range from 0.6–5.3 μm with a spectral resolution of $R \sim 100$, across the $3'' \times 3''$ FoV. We estimate the NIRSpec IFU PSF and LSF (Appendix A and B), in order to accurately study the quasar system.

Scaling relations based on the $H\alpha$ and $H\beta$ broad emission lines give a black hole mass $M_{BH} = (1.4^{+3.1}_{-1.0}) \times 10^9 M_{\odot}$, implying a high accretion rate over its history. However, NDWFS J1425+3254 is currently accreting below the Eddington limit, with $L_{Bol}/L_{Edd} = 0.3^{+0.6}_{-0.2}$. The quasar’s spectrum around [O III] $\lambda\lambda 4959, 5007$ implies that there may be a quasar-driven outflow with velocity $6050^{+460}_{-630} \text{ km s}^{-1}$. This may be one of the most extreme outflows in the early Universe. The stellar mass of the quasar host galaxy cannot be determined because of the quasar’s light, but based on the black hole–stellar mass relation the host is likely to have $M_* \approx 10^{10}$ – $10^{11} M_{\odot}$. The quasar host likely has a significant amount of obscured star formation, with a measured SFR of $<(46.1 \pm 14.5) M_{\odot} \text{ yr}^{-1}$ increasing to $<1600 M_{\odot} \text{ yr}^{-1}$ when corrected for dust attenuation.

The IFU observations reveal that NDWFS J1425+3254 is part of a complex, merging system. Other members of the system include two companion galaxies with projected separations of 5–8 kpc from the quasar host. The companion in the north has an older, very massive stellar population that is relatively metal-rich, with moderate ongoing star formation significantly below the star-forming main sequence. This companion has begun merging with the quasar host, and a clear bridge of hot, ionised gas connects the two galaxies. A second, distinct merger is ongoing from the south, with a companion galaxy that is younger and less massive than the northern one. The southern companion likely has greater ongoing star formation than the northern one, lying on the star-forming main sequence, but remains metal-poor. Both companions and the gas bridge are likely photoionised by the central quasar. With two separate galaxies merging into the quasar host, this is a “train-wreck” merger in progress. These ongoing mergers may have triggered both the ongoing star formation and the intense quasar activity.

Finally, there is a potential foreground galaxy at $z = 1.135$, located $0''.81$ from the quasar. This galaxy should act as a gravitational lens to the background quasar giving a magnification of $1 < \mu < 2$, <0.75 mag. The discovery of this source was enabled by the $R \sim 100$ prism spectra, which sacrifices spectral resolution to cover the full NIRSpec wavelength range of 0.6–5.3 μm in a single exposure. High- z quasar studies that use the $R \sim 2700$ grating provide more accurate kinematic measurements, more ideal for studying the $H\beta$ – $H\alpha$ emission lines (e.g., Marshall et al. 2023, 2024; Liu et al. 2024; Decarli et al. 2024; Loiacono et al. 2024). However, the typical G395M/F290LP mode produces a spectrum only from 2.9 to 5.3 μm that would have missed the foreground source’s emission lines at 1–1.5 μm . The prism spec-

tra also allowed for detections of the continuum emission from the companion galaxies across the rest-frame UV and optical, that would have been too faint to detect in $R \sim 2700$ spectra with equivalent exposure time, thus enabling SED fitting and stellar mass estimates. Taking $R \sim 2700$ spectra across the full 0.6–5.3 μm wavelength range, deep enough to detect the continuum emission, would require significantly more observing time.

This superb data has revealed a potential extreme quasar-driven outflow, multiple companions and a gas bridge, and a likely foreground galaxy lens. Nevertheless, higher-resolution observations would be ideal for studying in greater detail the kinematics of this extreme “train-wreck” merging-quasar system.

Acknowledgements. We dedicate this paper to the memory of our colleague Glenn Schneider, a champion of high-contrast imaging across the Universe from solar eclipses to high- z quasars. We are extremely grateful to our Program NIRSpec Reviewer Alaina Henry and Program Coordinator Tony Roman, who were critical in ensuring that these observations were successfully executed. We thank Glenn Wahlgren and the JWST Help Desk team for their help understanding the NIRSpec LSF. We thank Alex Cameron for advice on using pPXF. This work is based on observations made with the NASA/ESA/CSA James Webb Space Telescope. The data were obtained from the Mikulski Archive for Space Telescopes at the Space Telescope Science Institute, which is operated by the Association of Universities for Research in Astronomy, Inc., under NASA contract NAS 5-03127 for JWST. These observations are associated with JWST program 1176 as part of the Prime Extragalactic Areas for Reionization and Lensing Science (PEARLS) GTO program. MAM acknowledges support by the Laboratory Directed Research and Development program of Los Alamos National Laboratory under project number 20240752PRD1. RAW, SHC, and RAJ acknowledge support from NASA JWST Interdisciplinary Scientist grants NAG5-12460, NNX14AN10G and 80NSSC18K0200 from GSFC. Work by CJC and NJA acknowledge support from the European Research Council (ERC) Advanced Investigator Grant EPOCHS (788113). CNAW acknowledges funding from the JWST/NIRCam contract NASS-0215 to the University of Arizona. CC is supported by the National Natural Science Foundation of China, No. 11803044, 11933003, 12173045, the Chinese Academy of Sciences (CAS), through a grant to the CAS South America Center for Astronomy (CASSACA), and the China Manned Space Project with grant NO. CMS-CSST-2021-A05. AZ acknowledges support by the Ministry of Science & Technology, Israel, and by Grant No. 2020750 from the United States-Israel Binational Science Foundation (BSF) and Grant No. 2109066 from the United States National Science Foundation (NSF). GF and JSBW were supported by the Australian Research Council Centre of Excellence for All Sky Astrophysics in 3 Dimensions (ASTRO 3D), through project CE170100013 MP acknowledges grant PID2021-127718NB-I00 funded by the Spanish Ministry of Science and Innovation/State Agency of Research (MICIN/AEI/10.13039/501100011033), and the grant RYC2023-044853-I, funded by MICIU/AEI/10.13039/501100011033 and FSE+. HÜ acknowledges support through the ERC Starting Grant 101164796 “APEX”. This research has made use of NASA’s Astrophysics Data System, and QFitsView, developed by Smithsonian Astrophysical Observatory. This paper made use of Python packages and software AstroPy (Astropy Collaboration et al. 2013), JWST (Bushouse et al. 2022), MATPLOTLIB (Hunter 2007), NUMPY (van der Walt et al. 2011), PANDAS (Pandas Development Team 2020), PHOTUTILS (Bradley et al. 2018), REGIONS (Bradley et al. 2022), SciPy (Virtanen et al. 2020), SEABORN (Waskom 2021), SPECTRAL CUBE (Ginsburg et al. 2019), QDEBLEND3D (Husemann et al. 2013, 2014), QUBESPEC³, and WEBBPSF (Perrin et al. 2015).

References

- Abazajian, K. N., Adelman-McCarthy, J. K., Agüeros, M. A., et al. 2009, *ApJS*, 182, 543
- Araujo, B. L. C., Storchi-Bergmann, T., Rembold, S. B., Kaipper, A. L. P., & Dall’Agnol de Oliveira, B. 2023, *MNRAS*, 522, 5165
- Arribas, S., Perna, M., Rodríguez Del Pino, B., et al. 2024, *A&A*, 688, A146
- Asada, Y., Sawicki, M., Desprez, G., et al. 2023, *MNRAS*, 523, L40
- Astropy Collaboration, Robitaille, T. P., Tollerud, E. J., et al. 2013, *A&A*, 558, A33
- Baldwin, J. A., Phillips, M. M., & Terlevich, R. 1981, *PASP*, 93, 5
- Bañados, E., Schindler, J.-T., Venemans, B. P., et al. 2022, *ApJS*, 265, 29
- Bañados, E., Venemans, B., Walter, F., et al. 2013, *ApJ*, 773, 178
- Bañados, E., Venemans, B. P., Decarli, R., et al. 2016, *ApJS*, 227, 11
- Bañados, E., Venemans, B. P., Mazzucchelli, C., et al. 2018, *Nat*, 553, 473
- Barth, A. J., Martini, P., Nelson, C. H., & Ho, L. C. 2003, *ApJ Letters*, 594, L95
- ³ <https://github.com/honzascho1tz/Qubespec>

- Bessiere, P. S., Tadhunter, C. N., Ramos Almeida, C., & Villar Martín, M. 2012, *MNRAS*, 426, 276
- Binney, J. & Tremaine, S. 1987, *Galactic dynamics* (Princeton, N.J.: Princeton University Press)
- Bouwens, R. J., Illingworth, G. D., Oesch, P., et al. 2012, *ApJ*, 754, 83
- Boylan-Kolchin, M., Ma, C.-P., & Quataert, E. 2008, *MNRAS*, 383, 93
- Bradley, L., Deil, C., Ginsburg, A., et al. 2022, *astropy/regions*: v0.7
- Bradley, L., Sipocz, B., Robitaille, T., et al. 2018, *astropy/photutils*: v0.5
- Bushouse, H., Eisenhamer, J., Dencheva, N., et al. 2022, *JWST Calibration Pipeline*
- Byrne-Mamahit, S., Hani, M. H., Ellison, S. L., Quai, S., & Patton, D. R. 2023, *MNRAS*, 519, 4966
- Byrne-Mamahit, S., Patton, D. R., Ellison, S. L., et al. 2024, *MNRAS*, 528, 5864
- Böker, T., Arribas, S., Lützgendorf, N., et al. 2022, *A&A*, 661, A82
- Calzetti, D., Armus, L., Bohlin, R. C., et al. 2000, *ApJ*, 533, 682
- Cameron, A. J., Saxena, A., Bunker, A. J., et al. 2023, *A&A*, 677, A115
- Cappellari, M. 2017, *MNRAS*, 466, 798
- Cappellari, M. 2023, *MNRAS*, 526, 3273
- Cappellari, M. & Emsellem, E. 2004, *PASP*, 116, 138
- Carniani, S., Marconi, A., Maiolino, R., et al. 2015, *A&A*, 580, A102
- Champagne, J. B., Wang, F., Zhang, H., et al. 2024, *arXiv e-prints* [arXiv:2410.03826]
- Cho, H., Woo, J.-H., Wang, S., et al. 2023, *ApJ*, 953, 142
- Cisternas, M., Jahnke, K., Inskip, K. J., et al. 2011, *ApJ*, 726, 57
- Conroy, C. & Gunn, J. E. 2010, *ApJ*, 712, 833
- Conroy, C., Gunn, J. E., & White, M. 2009, *ApJ*, 699, 486
- Cool, R. J., Kochanek, C. S., Eisenstein, D. J., et al. 2006, *AJ*, 132, 823
- da Silva, R. L., Prochaska, J. X., Rosario, D., Tumlinson, J., & Tripp, T. M. 2011, *ApJ*, 735, 54
- Dalla Bontà, E., Peterson, B. M., Bentz, M. C., et al. 2020, *ApJ*, 903, 112
- Dalla Bontà, E., Peterson, B. M., Grier, C. J., et al. 2024, *arXiv e-prints*, arXiv:2410.21387
- de Graaff, A., Rix, H.-W., Carniani, S., et al. 2024, *A&A*, 684, A87
- De Rosa, G., Decarli, R., Walter, F., et al. 2011, *ApJ*, 739, 56
- Decarli, R., Dotti, M., Bañados, E., et al. 2019, *ApJ*, 880, 157
- Decarli, R., Loiacono, F., Farina, E. P., et al. 2024, *A&A*, 689, A219
- Decarli, R., Walter, F., Venemans, B. P., et al. 2017, *Nature*, 545, 457
- D'Eugenio, F., Pérez-González, P. G., Maiolino, R., et al. 2024, *Nature Astronomy* [arXiv:2308.06317]
- Díaz-Santos, T., Assef, R. J., Blain, A. W., et al. 2018, *Science*, 362, 1034
- Dojčinović, I., Kovačević-Dojčinović, J., & Popović, L. Č. 2023, *Advances in Space Research*, 71, 1219
- Domínguez, A., Siana, B., Henry, A. L., et al. 2013, *ApJ*, 763, 145
- Dong, X., Wang, T., Wang, J., et al. 2008, *MNRAS*, 383, 581
- Doyon, R., Joseph, R. D., & Wright, G. S. 1994, *ApJ*, 421, 101
- Duan, Q., Conselice, C. J., Li, Q., et al. 2024a, *arXiv e-prints*, arXiv:2407.09472
- Duan, Q., Li, Q., Conselice, C. J., et al. 2024b, *arXiv e-prints*, arXiv:2411.04944
- Duncan, K., Conselice, C. J., Mundy, C., et al. 2019, *ApJ*, 876, 110
- Dunlop, J. S., McLure, R. J., Robertson, B. E., et al. 2012, *MNRAS*, 420, 901
- Eilers, A.-C., Hennawi, J. F., Decarli, R., et al. 2020, *ApJ*, 900, 37
- Eilers, A.-C., Mackenzie, R., Pizzati, E., et al. 2024, *ApJ*, 974, 275
- Ellison, S. L., Patton, D. R., Mendel, J. T., & Scudder, J. M. 2011, *MNRAS*, 418, 2043
- Euclid Collaboration, Paterson, K., Schirmer, M., et al. 2023, *A&A*, 674, A172
- Fan, X., Narayanan, V. K., Lupton, R. H., et al. 2001, *AJ*, 122, 2833
- Fan, X., Strauss, M. A., Schneider, D. P., et al. 2003, *AJ*, 125, 1649
- Fan, X., White, R. L., Davis, M., et al. 2000, *AJ*, 120, 1167
- Farina, E. P., Schindler, J.-T., Walter, F., et al. 2022, *ApJ*, 941, 106
- Farina, E. P., Venemans, B. P., Decarli, R., et al. 2017, *ApJ*, 848, 78
- Ferland, G. J. & Netzer, H. 1983, *ApJ*, 264, 105
- Finkelstein, S. L., Papovich, C., Ryan, R. E., et al. 2012, *ApJ*, 758, 93
- Fujimoto, S., Ouchi, M., Kohno, K., et al. 2024, *arXiv e-prints*, arXiv:2402.18543
- Gardner, J. P., Mather, J. C., Abbott, R., et al. 2023, *PASP*, 135, 068001
- Gardner, J. P., Mather, J. C., Clampin, M., et al. 2006, *SSRv*, 123, 485
- Ginsburg, A., Koch, E., Robitaille, T., et al. 2019, *radio-astro-tools/spectral-cube*: Release v0.4.5
- Girelli, G., Pozzetti, L., Bolzonella, M., et al. 2020, *A&A*, 634, A135
- Glikman, E., Simmons, B., Mailly, M., et al. 2015, *ApJ*, 806, 218
- Goto, T., Utsumi, Y., Kikuta, S., et al. 2017, *MNRAS: Letters*, 470, L117
- Greene, J. E. & Ho, L. C. 2005, *ApJ*, 630, 122
- Greene, J. E., Labbe, I., Goulding, A. D., et al. 2024, *ApJ*, 964, 39
- Greene, J. E., Strader, J., & Ho, L. C. 2020, *ARA&A*, 58, 257
- Halpern, J. P. & Steiner, J. E. 1983, *ApJ*, 269, L37
- Hernquist, L. & Mihos, J. C. 1995, *ApJ*, 448, 41
- Hinshaw, G., Larson, D., Komatsu, E., et al. 2013, *ApJS*, 208, 19
- Hopkins, P. F., Hernquist, L., Cox, T. J., et al. 2006, *ApJS*, 163, 1
- Hummer, D. G. & Storey, P. J. 1987, *MNRAS*, 224, 801
- Hunter, J. D. 2007, *CiSE*, 9, 90
- Husemann, B., Jahnke, K., Sánchez, S. F., et al. 2014, *MNRAS*, 443, 755
- Husemann, B., Wisotzki, L., Sánchez, S. F., & Jahnke, K. 2013, *A&A*, 549, A43
- Isobe, Y., Ouchi, M., Nakajima, K., et al. 2023, *ApJ*, 956, 139
- Izumi, T., Matsuoka, Y., Onoue, M., et al. 2024, *ApJ*, 972, 116
- Ji, X., Übler, H., Maiolino, R., et al. 2024, *MNRAS*, 535, 881
- Jiang, C. Y., Jing, Y. P., Faltenbacher, A., Lin, W. P., & Li, C. 2008, *ApJ*, 675, 1095
- Jiang, L., Cohen, S. H., Windhorst, R. A., et al. 2020, *ApJ*, 889, 90
- Jiang, L., Egami, E., Mechtley, M., et al. 2013, *ApJ*, 772, 99
- Jiang, L., Fan, X., Ivezić, Ž., et al. 2007, *ApJ*, 656, 680
- Jones, G. C., Übler, H., Perna, M., et al. 2024, *A&A*, 682, A122
- Juodžbalis, I., Maiolino, R., Baker, W. M., et al. 2024, *arXiv e-prints*, arXiv:2403.03872
- Kacharov, N., Neumayer, N., Seth, A. C., et al. 2018, *MNRAS*, 480, 1973
- Kashikawa, N., Ishizaki, Y., Willott, C. J., et al. 2015, *ApJ*, 798, 28
- Kashino, D., Lilly, S. J., Matthee, J., et al. 2023, *ApJ*, 950, 66
- Kaspi, S., Smith, P. S., Netzer, H., et al. 2000, *ApJ*, 533, 631
- Kauffmann, G., Heckman, T. M., Tremonti, C., et al. 2003, *MNRAS*, 346, 1055
- Keel, W. C. 1996, *AJ*, 111, 696
- Keel, W. C., Bennert, V. N., Pancoast, A., et al. 2019, *MNRAS*, 483, 4847
- Keel, W. C., Chojnowski, S. D., Bennert, V. N., et al. 2012a, *MNRAS*, 420, 878
- Keel, W. C., Lintott, C. J., Schawinski, K., et al. 2012b, *AJ*, 144, 66
- Kennicutt, R. C. & Evans, N. J. 2012, *ARA&A*, 50, 531
- Kewley, L. J., Dopita, M. A., Sutherland, R. S., Heisler, C. A., & Trevena, J. 2001, *ApJ*, 556, 121
- Kocevski, D. D., Faber, S. M., Mozena, M., et al. 2012, *ApJ*, 744, 148
- Kokorev, V., Fujimoto, S., Labbe, I., et al. 2023, *ApJ*, 957, L7
- Kovacevic, J., Popovic, L. C., & Dimitrijevic, M. S. 2010, *ApJS*, 189, 15
- Kroupa, P. 2001, *MNRAS*, 322, 231
- Kuo, C.-Y., Lim, J., Tang, Y.-W., & Ho, P. T. P. 2008, *ApJ*, 679, 1047
- Kuraszkiewicz, J. K., Green, P. J., Forster, K., et al. 2002, *ApJS*, 143, 257
- Kurk, J. D., Walter, F., Fan, X., et al. 2007, *ApJ*, 669, 32
- Kurtz, M. J. & Mink, D. J. 1998, *PASP*, 110, 934
- Lamperti, I., Arribas, S., Perna, M., et al. 2024, *arXiv e-prints*, arXiv:2406.10348
- Larson, R. L., Finkelstein, S. L., Kocevski, D. D., et al. 2023, *ApJ*, 953, L29
- Lim, J. & Ho, P. T. P. 1999, *ApJ*, 510, L7
- Lintott, C. J., Schawinski, K., Keel, W., et al. 2009, *MNRAS*, 399, 129
- Litke, K. C., Marrone, D. P., Spilker, J. S., et al. 2019, *ApJ*, 870, 80
- Liu, W., Fan, X., Yang, J., et al. 2024, *ApJ*, 976, 33
- Loiacono, F., Decarli, R., Mignoli, M., et al. 2024, *A&A*, 685, A121
- Maiolino, R., Scholtz, J., Curtis-Lake, E., et al. 2023, *arXiv e-prints*, arXiv:2308.01230
- Marconini, C., D'Eugenio, F., Maiolino, R., et al. 2024, *arXiv e-prints*, arXiv:2411.08627
- Marian, V., Jahnke, K., Mechtley, M., et al. 2019, *ApJ*, 882, 141
- Marshall, M. A., Mechtley, M., Windhorst, R. A., et al. 2020, *ApJ*, 900, 21
- Marshall, M. A., Perna, M., Willott, C. J., et al. 2023, *A&A*, 678, A191
- Marshall, M. A., Yue, M., Eilers, A.-C., et al. 2024, *arXiv e-prints*, arXiv:2410.11035
- Matsuoka, Y., Izumi, T., Onoue, M., et al. 2024, *ApJ*, 965, L4
- Matsuoka, Y., Onoue, M., Kashikawa, N., et al. 2018, *PASJ*, 70
- Matthee, J., Naidu, R. P., Brammer, G., et al. 2024, *ApJ*, 963, 129
- Mazzucchelli, C., Decarli, R., Farina, E. P., et al. 2019, *ApJ*, 881, 163
- McElwain, M. W., Feinberg, L. D., Perrin, M. D., et al. 2023, *PASP*, 135, 058001
- McGreer, I. D., Fan, X., Strauss, M. A., et al. 2014, *AJ*, 148, 73
- Mechtley, M. 2014, PhD thesis, Arizona State University
- Mechtley, M. 2016, *psfMC*
- Mechtley, M., Jahnke, K., Windhorst, R. A., et al. 2016, *ApJ*, 830, 156
- Mechtley, M., Windhorst, R. A., Ryan, R. E., et al. 2012, *ApJ*, 756, L38
- Mérida, R. M., Gaspar, G., Sawicki, M., et al. 2025, *arXiv e-prints*, arXiv:2501.17925
- Merluzzi, P., Busarello, G., Dopita, M. A., et al. 2018, *ApJ*, 852, 113
- Mignoli, M., Gilli, R., Decarli, R., et al. 2020, *A&A*, 642, L1
- Mihos, J. C. & Hernquist, L. 1996, *ApJ*, 464, 641
- Moiseev, A. V., Smirnova, A. A., & Movsessian, T. A. 2023, *Universe*, 9, 493
- Moran, E. C., Halpern, J. P., Bothun, G. D., & Becker, R. H. 1992, *AJ*, 104, 990
- Morselli, L., Mignoli, M., Gilli, R., et al. 2014, *A&A*, 568, A1
- Nanayakkara, T., Glazebrook, K., Jacobs, C., et al. 2024, *Scientific Reports*, 14, 3724
- Neeleman, M., Bañados, E., Walter, F., et al. 2019, *ApJ*, 882, 10
- Oh, S. H., Kim, W.-T., Lee, H. M., & Kim, J. 2008, *ApJ*, 683, 94
- Osterbrock, D. E. 1989, *Astrophysics of gaseous nebulae and active galactic nuclei* (Mill Valley, Calif.: University Science Books)
- Pandas Development Team. 2020, *pandas-dev/pandas*: Pandas
- Park, D., Barth, A. J., Ho, L. C., & Laor, A. 2022, *ApJS*, 258, 38
- Parlanti, E., Carniani, S., Übler, H., et al. 2024a, *A&A*, 684, A24
- Parlanti, E., Carniani, S., Venturi, G., et al. 2024b, *arXiv e-prints*, arXiv:2407.19008
- Patton, D. R., Wilson, K. D., Metrow, C. J., et al. 2020, *MNRAS*, 494, 4969
- Perna, M., Arribas, S., Lamperti, I., et al. 2023a, *arXiv e-prints*, arXiv:2310.03067
- Perna, M., Arribas, S., Marshall, M., et al. 2023b, *A&A*, 679, A89

- Perrin, M. D., Long, J., Sivaramakrishnan, A., et al. 2015, *WebbPSF: James Webb Space Telescope PSF Simulation Tool*
- Perrotta, S., Hamann, F., Zakamska, N. L., et al. 2019, *MNRAS*, 488, 4126
- Popesso, P., Concas, A., Cresci, G., et al. 2023, *MNRAS*, 519, 1526
- Protušová, K., Bosman, S. E. I., Wang, F., et al. 2024, arXiv e-prints, arXiv:2412.12256
- Rauscher, B. J. 2024, *PASP*, 136, 015001
- Reed, D., Gardner, J., Quinn, T., et al. 2003, *MNRAS*, 346, 565
- Rigby, J., Hutchison, T. A., Rivera-Thorsen, T. E., et al. 2024, *JWST- Templates/Notebooks*
- Rigby, J. R., Vieira, J. D., Phadke, K. A., et al. 2023, arXiv e-prints, arXiv:2312.10465
- Rodríguez Del Pino, B., Perna, M., Arribas, S., et al. 2024, *A&A*, 684, A187
- Runnoe, J. C., Brotherton, M. S., & Shang, Z. 2012a, *MNRAS*, 427, 1800
- Runnoe, J. C., Brotherton, M. S., & Shang, Z. 2012b, *MNRAS*, 422, 478
- Salpeter, E. E. 1955, *ApJ*, 121, 161
- Sanders, D. B., Soifer, B. T., Elias, J. H., et al. 1988, *ApJ*, 325, 74
- Schawinski, K., Evans, D. A., Virani, S., et al. 2010, *ApJ*, 724, L30
- Schirmer, M., Diaz, R., Holhjem, K., Levenson, N. A., & Winge, C. 2013, *ApJ*, 763, 60
- Scholtz, J., Maiolino, R., D'Eugenio, F., et al. 2024, arXiv e-prints, arXiv:2311.18731
- Shah, E. A., Kartaltepe, J. S., Magagnoli, C. T., et al. 2022, *ApJ*, 940, 4
- Shen, Y., Richards, G. T., Strauss, M. A., et al. 2011, *ApJS*, 194, 45
- Shen, Y., Wu, J., Jiang, L., et al. 2019, *ApJ*, 873, 35
- Shuntov, M., McCracken, H. J., Gavazzi, R., et al. 2022, *A&A*, 664, A61
- Simpson, C., Mortlock, D., Warren, S., et al. 2014, *MNRAS*, 442, 3454
- Slob, M., Kriek, M., Beverage, A. G., et al. 2024, *ApJ*, 973, 131
- Solimano, M., González-López, J., Aravena, M., et al. 2025, *A&A*, 693, A70
- Stasińska, G., Vale Asari, N., Wójtowicz, A., & Koziel-Wierzbowska, D. 2025, *A&A*, 693, A135
- Stiavelli, M., Djorgovski, S. G., Pavlovsky, C., et al. 2005, *ApJ*, 622, L1
- Storey, P. J. & Zeppen, C. J. 2000, *MNRAS*, 312, 813
- Sun, J. 2020, *Sun_Astro_Tools*, GitHub
- Tang, Y.-W., Kuo, C.-Y., Lim, J., & Ho, P. T. P. 2008, *ApJ*, 679, 1094
- Toomre, A. & Toomre, J. 1972, *ApJ*, 178, 623
- Trakhtenbrot, B., Lira, P., Netzer, H., et al. 2017, *ApJ*, 836, 8
- Tsukui, T., Wisnioski, E., Krumholz, M. R., & Battisti, A. 2023, *MNRAS*, 523, 4654
- Übler, H., D'Eugenio, F., Perna, M., et al. 2024a, *MNRAS*, 533, 4287
- Übler, H., Maiolino, R., Curtis-Lake, E., et al. 2023, *A&A*, 677, A145
- Übler, H., Maiolino, R., Pérez-González, P. G., et al. 2024b, *MNRAS*, 531, 355
- van der Walt, S., Colbert, S. C., & Varoquaux, G. 2011, *CiSE*, 13, 22
- Vayner, A., Díaz-Santos, T., Eisenhardt, P. R. M., et al. 2024, arXiv e-prints, arXiv:2412.02862
- Veilleux, S., Kim, D. C., & Sanders, D. B. 2002, *ApJS*, 143, 315
- Veilleux, S. & Osterbrock, D. E. 1987, *ApJS*, 63, 295
- Vestergaard, M. & Peterson, B. M. 2006, *ApJ*, 641, 689
- Villanueva, V., Herrera-Camus, R., González-López, J., et al. 2024, *A&A*, 691, A133
- Virtanen, P., Gommers, R., Oliphant, T. E., et al. 2020, *Nat. Methods*, 17, 261
- Wagg, J., Wiklind, T., Carilli, C. L., et al. 2012, *ApJ*, 752, L30
- Wandel, A., Peterson, B. M., & Malkan, M. A. 1999, *ApJ*, 526, 579
- Wang, F., Yang, J., Fan, X., et al. 2019, *ApJ*, 884, 30
- Wang, F., Yang, J., Hennawi, J. F., et al. 2023, arXiv e-prints [arXiv:2304.09894]
- Wang, R., Carilli, C. L., Neri, R., et al. 2010, *ApJ*, 714, 699
- Waskom, M. 2021, *JOSS*, 6, 3021
- White, R. L., Lubow, S. H., & Shiao, B. 2022, *AJ*, 164, 73
- Willott, C. J., Albert, L., Arzoumanian, D., et al. 2010, *AJ*, 140, 546
- Willott, C. J., Delorme, P., Reylé, C., et al. 2009, *AJ*, 137, 3541
- Willott, C. J., Percival, W. J., McLure, R. J., et al. 2005, *ApJ*, 626, 657
- Windhorst, R. A., Cohen, S. H., Jansen, R. A., et al. 2023, *AJ*, 165, 13
- Wright, A. E. 1972, *MNRAS*, 157, 309
- Xiao, M., Oesch, P. A., Elbaz, D., et al. 2024, *Nature*, 635, 311
- Yang, J., Fan, X., Gupta, A., et al. 2023, *ApJS*, 269, 27
- Yang, J., Wang, F., Fan, X., et al. 2020, *ApJ*, 897, L14
- Younger, J. D., Hayward, C. C., Narayanan, D., et al. 2009, *MNRAS*, 396, L66
- Yue, M., Eilers, A.-C., Simcoe, R. A., et al. 2024, *ApJ*, 966, 176
- Zamora, S., Venturi, G., Carniani, S., et al. 2024, arXiv e-prints, arXiv:2412.02751
- Zappacosta, L., Piconcelli, E., Fiore, F., et al. 2023, *A&A*, 678, A201
- Zheng, W., Overzier, R. A., Bouwens, R. J., et al. 2006, *ApJ*, 640, 574
- Zhu, Y., Bakx, T. J. L. C., Ikeda, R., et al. 2024, *RNAAS*, 8, 284
- 1 Los Alamos National Laboratory, Los Alamos, NM 87545, USA
 - 2 School of Earth and Space Exploration, Arizona State University, Tempe, AZ 85287-1404, USA
 - 3 School of Physics, University of Melbourne, Parkville, VIC 3010, Australia
 - 4 ARC Centre of Excellence for All Sky Astrophysics in 3 Dimensions (ASTRO 3D), Australia
 - 5 Center for Astrophysics | Harvard & Smithsonian, 60 Garden Street, Cambridge, MA, 02138, USA
 - 6 INAF – Istituto di Astrofisica Spaziale e Fisica cosmica (IASF) Milano, Via A. Corti 12, 20133 Milan, Italy
 - 7 Dept. of Physics and Astronomy, University of Alabama, Box 870324, Tuscaloosa, AL 35404, USA
 - 8 Center for Astrophysics | Harvard & Smithsonian, 60 Garden St., Cambridge, MA 02138 USA
 - 9 International Centre for Radio Astronomy Research (ICRAR) and the International Space Centre (ISC), The University of Western Australia, M468, 35 Stirling Highway, Crawley, WA 6009, Australia
 - 10 Space Telescope Science Institute, 3700 San Martin Drive, Baltimore, MD 21218, USA
 - 11 Association of Universities for Research in Astronomy (AURA) for the European Space Agency (ESA), STScI, Baltimore, MD 21218, USA
 - 12 Center for Astrophysical Sciences, Department of Physics and Astronomy, The Johns Hopkins University, 3400 N Charles St. Baltimore, MD 21218, USA
 - 13 Jodrell Bank Centre for Astrophysics, Alan Turing Building, University of Manchester, Oxford Road, Manchester M13 9PL, UK
 - 14 Instituto de Física de Cantabria (CSIC-UC). Avenida. Los Castros s/n. 39005 Santander, Spain
 - 15 Department of Astronomy/Steward Observatory, University of Arizona, 933 N Cherry Ave, Tucson, AZ, 85721-0009, USA
 - 16 Steward Observatory, University of Arizona, 933 N Cherry Ave, Tucson, AZ, 85721-0009, USA
 - 17 Department of Physics and Astronomy, University of Missouri, Columbia, MO 65211, USA
 - 18 Department of Astronomy, University of Maryland, College Park, 20742, USA
 - 19 Physics Department, Ben-Gurion University of the Negev, P.O. Box 653, Be'er-Sheva 8410501, Israel
 - 20 Jodrell Bank Centre for Astrophysics, University of Manchester, Oxford Road, Manchester, UK
 - 21 Chinese Academy of Sciences South America Center for Astronomy, National Astronomical Observatories, CAS, Beijing 100101, China
 - 22 Research School of Astronomy and Astrophysics, Australian National University, Canberra, ACT 2611, Australia
 - 23 Department of Physics, The University of Hong Kong, Pokfulam Road, Hong Kong
 - 24 Centro de Astrobiología (CAB), CSIC-INTA, Ctra. de Ajalvir km 4, Torrejón de Ardoz, E-28850, Madrid, Spain
 - 25 Max-Planck-Institut für extraterrestrische Physik, Gießenbachstraße 1, 85748 Garching, Germany
 - 26 National Research Council of Canada, Herzberg Astronomy & Astrophysics Research Centre, 5071 West Saanich Road, Victoria, BC V9E 2E7, Canada
 - 27 Kavli Institute for Cosmology, University of Cambridge, Madingley Road, Cambridge, CB3 0HA, UK
 - 28 Cavendish Laboratory - Astrophysics Group, University of Cambridge, 19 JJ Thomson Avenue, Cambridge, CB3 0HE, UK

Appendix A: Point Spread Function

Using QDeblend3D (Husemann et al. 2013, 2014), we determined the PSF shape by measuring the flux of the quasar BLR wings in each spaxel. As the PSF varies with wavelength, we measured these BLR fluxes for both the $H\beta$ and $H\alpha$ broad BLR lines. For $H\alpha$, we measured the flux across rest-frame 6485–6525 Å and 6605–6640 Å, i.e., both sides of the emission peak at 6564.6 Å. For $H\beta$, we measured the flux across rest-frame 4800–4850 Å, i.e., only on the blue side of the peak at 4862.68 Å, as the red side is contaminated by blending with $[O\ III]\ \lambda 4959$. Figure A.1 shows the resulting 2D $H\beta$ and $H\alpha$ BLR flux maps, that is, the IFU PSF shape at 3.35 and 4.52 μm . The FWHM of each PSF, averaged in the horizontal and vertical directions, is 0'':14 at 3.35 μm and 0'':18 at 4.52 μm . These measurements are consistent with the PSF FWHM measurements for the NIRSpect IFU from D'Eugenio et al. (2024).

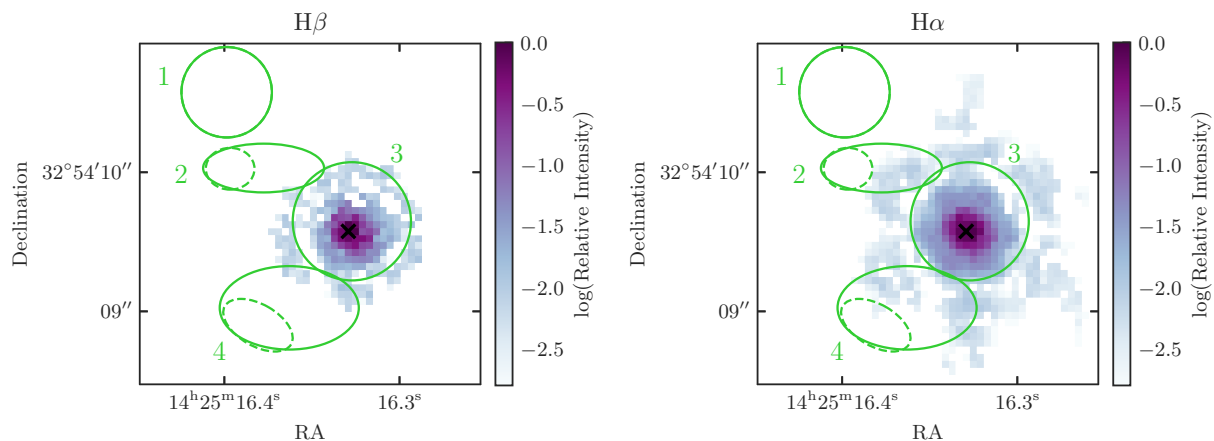


Fig. A.1. The NIRSpect IFU instrumental PSF at 3.35 μm as measured from the broad $H\beta$ line (left), and at 4.52 μm as measured from the broad $H\alpha$ line (right) of NDWFS J1425+3254. The coloured solid ellipses mark the emission line regions as in Figure 7, to assist in visualising the PSF scale. As Regions 2 and 4 overlap the quasar PSF, we redefine two alternate apertures, Regions 2* and 4*, within the original apertures but avoiding the region with quasar flux, shown as dashed ellipses. This is so that we can extract and model the continuum emission from these regions in Sections 2.3.5 and 4.3 without quasar contamination.

Appendix B: Line Spread Function

Throughout this analysis, we measured line FWHMs smaller than expected from the pre-flight estimate of the NIRSpect prism LSF ($R \sim 35\text{--}300$). Accurately measuring line widths and velocities requires a more accurate estimate of the in-flight LSF.

The compact planetary nebula SMP LMC 58 = IRAS 05248–7007 was observed in the JWST Commissioning and Calibration programs PID 1125 and 1492 to characterize the NIRSpect LSF (see e.g., Isobe et al. 2023, who performed a similar analysis on SMP LMC 58 NIRSpect data from other filter–grating pairs). We downloaded the IFU prism data from the planetary nebula from PID 1492, as reduced by the default MAST pipeline with calibration software version 1.14.0 and reference file JWST_1253.PMAP. We used the prism data from Observation 8, which has 4 dithers in a 4-point nod pattern and a total exposure time of 350 s. We integrated the spectrum across a circular aperture of radius 1'' surrounding the centre of the emission and subtracted the continuum to obtain a pure emission-line spectrum. We measured the FWHM of the planetary nebula's emission lines by fitting each with a Gaussian profile. We ignored lines with low S/N or blending with other lines, leaving nine emission lines from 0.6–4.3 μm . The emission lines of this planetary nebula were unresolved in VLT/X-shooter $R \sim 6500$ spectra from 1'':2 slits (Euclid Collaboration et al. 2023; Isobe et al. 2023) and therefore will be unresolved in this $R \sim 100$ spectra. We therefore assumed that the observed line width arises purely from instrumental broadening. Figure B.1 shows the measured instrumental FWHM as a function of wavelength. Uncertainties in $\text{FWHM}(\lambda)$ were calculated by assuming that each line's FWHM was measured with an uncertainty σ of half a wavelength element, $\sigma = 25\ \text{\AA}$.

Owing to the limited number of emission lines, we do not estimate the shape of $\text{FWHM}(\lambda)$. Instead, we use the shape of the spectral resolving power $R(\lambda)$ as estimated from the pre-flight data⁴, where $1/R \equiv \text{FWHM}/\lambda$. Using linear least squares, we find that the optimal solution for the constant α in $\text{FWHM}(\lambda) = \alpha \text{FWHM}_{\text{pre-flight}}(\lambda)$ is $\alpha = 0.873 \pm 0.079$. The uncertainties were calculated by assuming that the FWHM measurements are all $\sigma = 25\ \text{\AA}$ larger or smaller than our best estimates. Modifying the integration aperture by $\pm 50\%$ adds an additional uncertainty of ± 0.005 .

Translating these to measurements of the spectral resolving power, we find $R(\lambda) = \beta R_{\text{pre-flight}}(\lambda)$, where $\beta = 1/\alpha = 1.14^{+0.11}_{-0.09}$. That is, we measure a spectral resolution that is $14^{+11}_{-9}\%$ larger than the pre-flight expectations. Figure B.1 shows the resulting spectral resolving power as a function of wavelength. This factor of increase is broadly consistent with the assumed multiplication factors used in previous NIRSpect studies, for example, Greene et al. (2024) derived $\beta = 1.3$, and Slob et al. (2024) derived $\beta = 1.2$, although those were for the Micro-Shutter Assembly rather than the IFU. See also Isobe et al. (2023), de Graaff et al. (2024), and Nanayakkara et al. (2024) for measurements of the NIRSpect resolution for other observing modes and filter–disperser pairs.

⁴ as tabulated at <https://jwst-docs.stsci.edu/jwst-near-infrared-spectrograph/nirspect-instrumentation/nirspect-dispersers-and-filters>

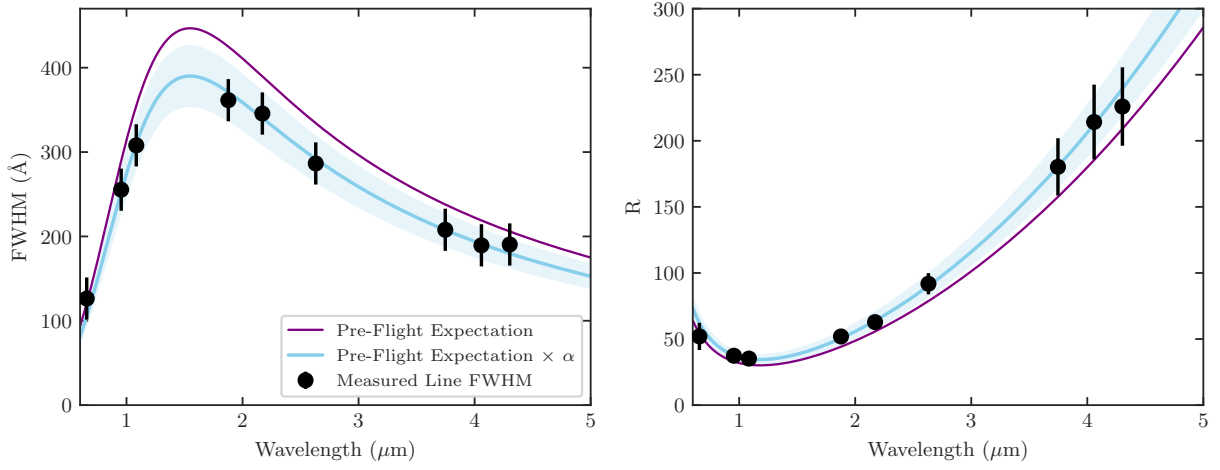


Fig. B.1. The NIRSpec IFU prism instrumental FWHM (left) as a function of wavelength. The purple curve shows the pre-flight estimates. The black points are measurements of emission lines from the planetary nebula SMP LMC 58, which have negligible intrinsic line width. The blue curve is the optimal scaling of the pre-flight expectation to match the observed measurements of the planetary nebula, with the shaded region showing the $\pm 1\sigma$ uncertainty. The right panel shows the corresponding spectral resolving power $R = \lambda/\text{FWHM}$.

The corresponding velocity resolution is $\text{FWHM}_{\text{inst}} = c/R$, where c is the speed of light. At the NDWFS J1425+3254 redshift of $z = 5.89$, the instrumental velocity resolutions for our key lines are $\text{FWHM}_{\text{inst}} = 2083 \pm 188 \text{ km s}^{-1}$, $1997 \pm 181 \text{ km s}^{-1}$, $1966 \pm 178 \text{ km s}^{-1}$, and $1126 \pm 102 \text{ km s}^{-1}$, for $\text{H}\beta$, $[\text{O III}]\lambda\lambda 4959, 5007$, and $\text{H}\alpha$ respectively. We assume that $\text{FWHM}_{\text{inst}, [\text{NII}]} = \text{FWHM}_{\text{inst}, \text{H}\alpha}$. The stated uncertainties are based on the uncertainties in α above.